Electronic Supplementary Material (ESI) for Chemical Science.

Electronic Supplemental Information (ESI) for:

Simplifying and expanding the scope of boron imidazolate framework (BIF) synthesis using mechanochemistry

Cameron B. Lennox,[a,b] Jean-Louis Do,[a,b] Joshua G. Crew,[a,c] Mihails Arhangelskis,[a,d] Hatem M. Titi,[a,b] Ashlee J. Howarth,[b,e,f] Omar K. Farha[f] and Tomislav Friščić[a,b*]

a. Department of Chemistry, McGill University, 801 Sherbrooke St. W. H3A 0B8 Montreal, Canada
b. FRQNT Quebec Centre for Advanced Materials (QCAM/CQMF), Montreal, Canada
c. School of Chemistry, Cardiff University, Main Building, Park Place, Cardiff CF10 3AT, UK
d. Faculty of Chemistry, University of Warsaw, 1 Pasteura St. 02-093 Warsaw, Poland
e. Department of Biochemistry and Chemistry, Concordia University, 7141 Sherbrooke St. W. H4B 1R6 Montreal, Canada
f. International Institute for Nanotechnology, Department of Chemistry, Northwestern University, 2145 Sheridan Road, 60208 Evanston, Il, United States

Table of Contents

S1 Materials and Methods

Unless otherwise indicated, all reagents and solvents were obtained from commercial sources and were used without further purification.

S1.1 Thermogravimetric analysis (TGA)

Thermogravimetric analysis (TGA) was performed utilizing approximately 5 mg of sample on a Mettler-Toledo TGA/DSC 1 system. The system was operated on a PC with STARe software. Samples were heated from 25 to 600 °C at a rate of 10 °C/min under constant air flow. The balance and purge flow were 40 mL/min and 25 mL/min respectively.

S1.2 Powder X-ray diffraction (PXRD)

Powder X-ray diffraction (PXRD) patterns were collected using a Bruker D2 Phaser powder diffractometer equipped with a Cu-Kα (λ = 1.5418 Å) source and Lynxeye detector. The patterns were collected in the angular region between 5° and 40° (2θ) with a step size of 0.05°. PXRD patterns used for structure solution-refinement were collected in the angular region between 3° and 70° (2θ) with a step size of 0.02° and 6.0 s acquisition time per step.

S1.4 Solid-state nuclear magnetic resonance (ssNMR) spectroscopy

The ^{13}C CPMAS spectrum was acquired in 512 scans under spinning at 8 kHz, using a recycle delay of 10 s with a contact time of 4 ms at a ^{13}C rf field of approximately 60 kHz. SPINAL-64 decoupling at a rf field of 90 kHz was applied during acquisition. Spectra were referenced using the carbonyl carbon signal in glycine at 176.4 ppm with respect to TMS.

S1.5 Solution nuclear magnetic resonance (NMR) spectroscopy

^{1}H NMR spectra were recorded on a Varian Inova 500MHz NMR spectrometer. Chemical shifts are reported relative to methanol-d$_4$ (δ 3.31) and data is presented as chemical shifts, and integration.

S1.6 Fourier-transform infrared attenuated total reflectance (FTIR-ATR) spectroscopy

Infrared spectra were obtained using a Bruker Platinum ATR spectrometer, and are reported in wavenumber (cm^{-1}) units.

S1.7 Inductively coupled plasma mass spectrometry (ICP-MS)

Analysis was performed on a FINNIGAN iCapQ SOLUTION ICP-MS, with samples pre-digested with 50% H_2O_2 and TMG HNO_3, before serial dilution to appropriate concentration for analysis. Calibration curves were prepared for Li-, Cu- and Ag-based materials, following standard operating procedures.

S1.8 Nitrogen porosity measurements

Nitrogen adsorption/desorption isotherms were recorded using a Micromeritics TriStar (II) instrument at 77 K for Li-BIF-3, Quantachrom instrument at 77 K for Cu-BIF-3 and a Micromeritics TriStar (II) Plus instrument at 77 K for Ag-BIF-3.

S1.9 Scaning electron microscopy

SEM images were recorded on a QUANTA FED 450 electron microscopy. Samples were loaded on carbon tape *via* dispersion in hexanes and were coated with 4nm Pt prior to measurement.

S2 Synthetic Procedures

All mechanochemical reactions were carried out in a Retsch MM200 mill operated at a frequency of 25 Hz, using a 15 mL stainless-steel milling jar charged with two stainless steel balls (7 mm, 1.37g) for Li- and Ag-based reactions, and in a 15 mL ZrO_2 jar charged with one ZrO_2 ball (10mm, 2.97g) for Cu-based reactions. Synthesis of H[B(**Im**)$_4$] and H[B(**Meim**)$_4$] were adapted from the literature[1] and their formation was confirmed *via* PXRD, NMR and FTIR-ATR analysis. ^{1}H-NMR of HB(**Im**)$_4$ CD_3OD: δ 7.59 (s, 1H), 6.26 (d, 1H), 6.07 (d, 1H). ^{1}H-NMR of HB(**Meim**)$_4$ CD_3OD: δ 1.80 (s, 12H), 6.75 (d, 4H), 7.06 (d, 4H).

S2.1 Synthesis of Li-BIF-1 (zni-topology) by milling

LiOH (0.6 mmol, 14 mg) was added to a 15 mL stainless-steel jar charged with two stainless steel balls (7mm, 1.37g). H[B(**Im**)$_4$] (0.6mmol, 168 mg) was added along with 45µL of MeCN (η = 0.25 µL mg^{-1}). The reaction mixture was milled for 60 minutes at 25 Hz. The MOF was activated by stirring in 15mL of MeCN for 18 hours, and evacuated at 80°C and 165 mmHg overnight.

S2.2 Synthesis of Cu-BIF-1 (zni-topology) by milling

Cu_2O (0.35mmol, 50 mg) was added to a 15 mL zirconia jar charged with one zirconia ball (10mm, 2.97g). H[B(**Im**)$_4$] (0.7mmol, 196mg) was added along with NH_4NO_3 (5% by weight) and 123 µL of MeOH (η=0.5 µL mg^{-1}). The reaction mixture was milled for 60 minutes at 25 Hz. The MOF was activated by stirring in 15mL of MeOH for 18 hours, and evacuated at 80°C and 165 mmHg overnight.

S2.3 Synthesis of Li-BIF-3 (SOD-topology) by milling

LiOH (0.5mmol, 12 mg) was added to a 15 mL stainless-steel jar charged with two stainless steel balls (7mm, 1.37g). H[B(**Meim**)$_4$] (0.5mmol, 170mg) was added along with 182 µL of a 3:1 by volume mixture of MeCN : **amb** (η = 1 µL mg^{-1}). The reaction mixture was milled for 60 minutes at 25 Hz. The MOF was activated by stirring in 15mL of MeCN for 18 hours, and evacuated at 80°C and 165 mmHg overnight.

S2.4 Synthesis of Li-BIF-2 (dia-topology) by milling

LiOH (0.5mmol, 12 mg) was added to a 15 mL stainless-steel jar charged with two stainless steel balls (7mm, 1.37g). H[B(**Meim**)$_4$] (0.5mmol, 170mg) was added along 91 µL of a 3:1 mixture by volume of MeCN : **amb** (η = 0.5 µL mg^{-1}). The reactant mixture was milled for 60 minutes. The reactant mixture was milled for 60 minutes. The MOF was activated by stirring in 15mL of MeCN for 18 hours, and evacuated at 80°C and 165 mmHg overnight.

S2.5 Synthesis of Cu-BIF-3 (SOD-topology) by milling

Cu_2O (0.35mmol, 50 mg) was added to a 15 mL zirconia jar charged with one zirconia ball (10mm, 2.97g). H[B(**Meim**)$_4$] (0.7mmol, 238mg) was added along with NH_4NO_3 (5% wt/wt) and 300 µL of MeOH (η = 1 µL mg^{-1}). The reaction mixture was milled for 60 minutes at 25 Hz. The resulting

MOF was activated by stirring in 15mL of MeCN for 18 hours, and evacuated at 80°C and 165 mmHg overnight.

S2.6 Synthesis of Cu-BIF-2 (dia-topology) by milling

Cu_2O (0.35mmol, 50 mg) was added to a 15 mL zirconia jar charged with one zirconia ball (10mm, 2.97g). H[B(**Meim**)$_4$] (0.7mmol, 238mg) was added along with NH_4NO_3 (5% wt/wt) and 150 µL of MeOH (η = 0.5 µL mg^{-1}). The reaction mixture was milled for 90 minutes at 25 Hz. The resulting MOF was activated by stirring in MeCN for 18 hours, and evacuated at 80°C and 165 mmHg overnight.

S2.7 Synthesis of Ag-BIF-3 (SOD-topology) by milling

$AgNO_3$ (0.25 mmol, 42.5 mg) and K_2CO_3 (0.125 mmol, 17.25 mg) were added to a 15 mL stainless steel jar charged with two stainless-steel balls (7 mm, 1.37g). One stoichiometric equivalent of H[B(**Meim**)$_4$] (0.25 mmol, 85 mg) was added, along with 36 µL of MeCN (η = 0.25 µL mg^{-1}). The reaction mixture was milled for 30 minutes at 25 Hz. The resulting MOF was activated by sequential washing in 15mL of cold MeOH for 30 minutes and acetone for 18 hours, and evacuated at 80°C and 165 mmHg overnight.

S2.8 Synthesis of Ag-BIF-2 (dia-topology) by milling

$AgNO_3$ (0.35 mmol, 59.5 mg) and K_2CO_3 (0.175 mmol, 24.12 mg) was added to a 15 mL stainless steel jar charged with two stainless-steel balls (7 mm, 1.37g). One stoichiometric equivalent of H[B(**Meim**)$_4$] (0.35 mmol, 119 mg) was added, along with 50 µL of MeCN (η = 0.25 µL mg^{-1}). The reaction mixture was milled for 60 minutes at 25 Hz. The resulting MOF was activated by sequential washing in 15mL of cold MeOH for 30 minutes and acetone for 18 hours, and evacuated at 80°C and 165 mmHg overnight.

S3 Computational methods

Periodic DFT calculations were performed using the plane-wave DFT code CASTEP 19.1.[2] The crystal structures of the dia- and SOD-polymorphs of Li- Cu- and Ag-BIFs were energy-minimized in order to calculate the energy difference between the polymorphs. The optimized crystal structures of Ag-BIF-2 and Ag-BIF-3 were used to calculate the ^{13}C ssNMR parameters.

S3.1 Geometry optimization

The experimental crystal structures were converted into CASTEP input format using the program cif2cell.[3] The calculations were performed using the PBE[4] functional combined with many-body dispersion (MBD*) semi-empirical dispersion correction scheme.[5-7] The plane-wave basis set was truncated at 700 eV plane-wave cut-off, with the on-the-fly generated ultrasoft pseudopotentials being used for attenuating the Coulomb potential in the core regions of electron density. The electronic 1st Brillouin zone was sampled with a $2\pi \times 0.07$ Å^{-1} Monkhorst-Pack k-point grid.[8]

The crystal structures were geometry-optimized with respect to atom positions and unit cell parameters, subject to the space group symmetry constraints. The calculation involved the following convergence criteria: total energy change 2×10^{-5} eV/atom; maximum atomic force 0.05 eV/Å; maximum atomic shift 10^{-3} Å; maximum stress tensor component 0.05 GPa.

S3.2 ssNMR relative chemical shift calculations

The optimized structures of Ag-BIFs were used for ssNMR calculations. The NMR shielding tensors were calculated using the Gauge Including Projector Augmented Waves (GIPAW)[9] method implemented in CASTEP.[2] Compared to geometry optimization, a higher plane wave cutoff of 1000 eV was used, the FT standard and fine grid scales were set to 2.0 and 3.0, respectively. The isotropic ^{13}C NMR shieldings were converted into chemical shifts using the reference shielding of 171 ppm.

S3.3 Accessible void calculations

Theoretical accessible surface area was calculated using *MOF Explorer* (https://mausdin.github.io/MOFsite/index.html) with 200 probes per atom, and with a diameter of 3.72Å (model for N_2).

S4 X-ray Diffraction, with selected results of mechanochemical reaction screening

S4.1 Crystal structure analysis of Ag-BIFs from powder X-ray diffraction data

Due to the lack of suitable single crystals of Ag-BIF-2 and Ag-BIF-3, their crystal structures had to be determined from PXRD data. The powder patterns were indexed using the DICVOL06[10] algorithm and the space groups were determined by analyzing individual diffraction intensities extracted using the Le Bail method,[11] implemented in EXPO2014 software. The simulated annealing structure solution and Rietveld refinement[12] were performed with TOPAS Academic 6.[13] The PXRD pattern of Ag-BIF-2 did not match any of the BIF structures reported in CSD, therefore *ab initio* crystal structure determination had to be performed. The diffractogram was indexed with a monoclinic cell with $P2_1$ symmetry. The unit cell volume of 934 Å^3 suggested the unit cell content of Ag_2B_2(**Meim**)$_8$, therefore the asymmetric unit was expected to contain 1xAg, 1xB and 4x**Meim** species. The structure determination in TOPAS was started with Pawley refinement,[14] during which the unit cell parameters were refined along with the pseudo-Voigt peak shape parameters, Chebyshev 6-term polynomial function and zero error parameter. The values of these parameters were subsequently fixed for the duration of the Simulated annealing procedure, during which the individual Ag and B atom along with four symmetry-independent **Meim** rigid body fragments were allowed to freely move within the unit cell. The structure solution resulted in a **dia**-topology framework, with both B and Ag atoms each coordinated with four imidazolate linkers, as expected for a BIF structure. In order to obtain more accurate geometric parameters, the structure was geometry-optimized in CASTEP[2] (see section S 3.1), with the DFT-optimized geometry used as a starting model for Rietveld refinement. During Rietveld refinement of Ag-BIF-2 structure, positions of Ag and B atoms, as well as positions and orientations of the symmetry-independent **Meim** linkers were freely refined, with the atomic thermal motion characterized by a single isotropic Debye-Waller factor. In addition, all parameters constrained during simulated annealing (zero shift, peak shape and background polynomial) were also allowed to refine. Owing to a large number of refinable parameters in the structural model, bond and angle restraints were added to preserve the coordination geometry around the Ag and B nodes. In the case of Ag-BIF-3, the material was found to be isostructural with the previously published Cu-BIF-3 (CSD MUCLOM), therefore this structure was used as a starting model for Rietveld refinement, with the Cu node replaced by the Ag atom. The refinement parameters for Ag-BIF-2 and Ag-BIF-3 structures are shown in Table S1.

Table S1. Crystallographic parameters of Ag-BIF structures determined from powder x-ray diffraction data.

	Ag-BIF-2	Ag-BIF-3
Formula	$AgB(C_4H_5N_2)_2$	$AgB(C_4H_5N_2)_2$
M_r (g mol^{-1})	280.87	208.87
Crystal system	monoclinic	cubic
a / Å	7.5198(4)	16.6659(3)
b / Å	16.3763(9)	16.6659(3)
c / Å	7.5876(4)	16.6659(3)
α (°)	90	90
β (°)	90.136(6)	90
γ (°)	90	90
V / Å^3	934.38(9)	4629.0(2)
Z	2	6
Space group	$P2_1$	$P\bar{4}3n$
ρ_c (g cm^{-3})	1.575	0.954
Radiation type	CuK_α	CuK_α
$F(000)$	448	1344
R_{wp}	0.090	0.076
R_p	0.068	0.060
R_{Bragg}	0.029	0.031
χ^2	2.960	3.143
CCDC number	2081806	2081807

S4.2 Crystal structure analysis for [Hamb$^+$][B(Meim)$_4^-$]·2H$_2$O using single crystal X-ray diffraction

Single crystal X-ray diffraction data were measured on a Bruker D8 Venture diffractometer equipped with a Photon 200 area detector, and *IμS* microfocus X-ray source (Bruker AXS, Cu*K*α source). All measurements were carried out at room temperature in which crystals coated with a thin layer of amorphous oil. Data were collected in a series of *φ*- and *ω*-scans. APEX3 software was used for data collection, integration and reduction.[15] Multi-scan absorption correction was applied using SADABS-2016/2.[16] Structure solution was carried out using the SHELXTL package from Bruker.[17] The parameters were refined for all data by full-matrix-least-squares or F^2 using SHELXL.[18] All of the nonhydrogen atoms were refined with anisotropic thermal parameters. All hydrogen atom thermal parameters were constrained to ride on the carrier atom. The structure was found to be twinned by inversion. Crystallographic data in CIF format have been deposited with the Cambridge Crystallographic Data Centre (CCDC deposition code 2084944).

S4.3 Experimental powder X-ray diffraction (PXRD) patterns illustrating mechanochemical reaction screening

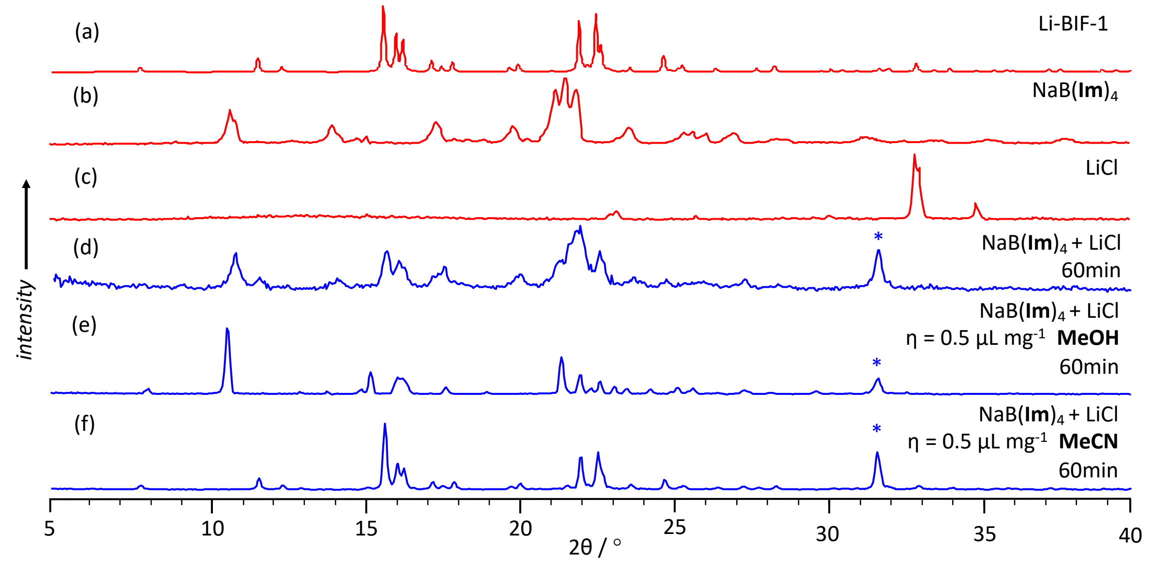

Figure S1. Selected PXRD patterns for neat grinding and LAG of Na[B(**Im**)$_4$] and LiCl to give Li-BIF-1: (a) Li-BIF-1 (MOXJEP), (b) Na[B(**Im**)$_4$], (c) LiCl, (d) neat milling of LiCl and Na[B(**Im**)$_4$]. Reaction product following LAG with: (e) MeOH (0.50 µL mg^{-1}), or (f) MeCN (0.5 µL mg^{-1}) for 60 minutes. PXRD analysis indicates complete conversion to Li-BIF-1 and NaCl. The asterisk highlights a characteristic Bragg reflection of NaCl.

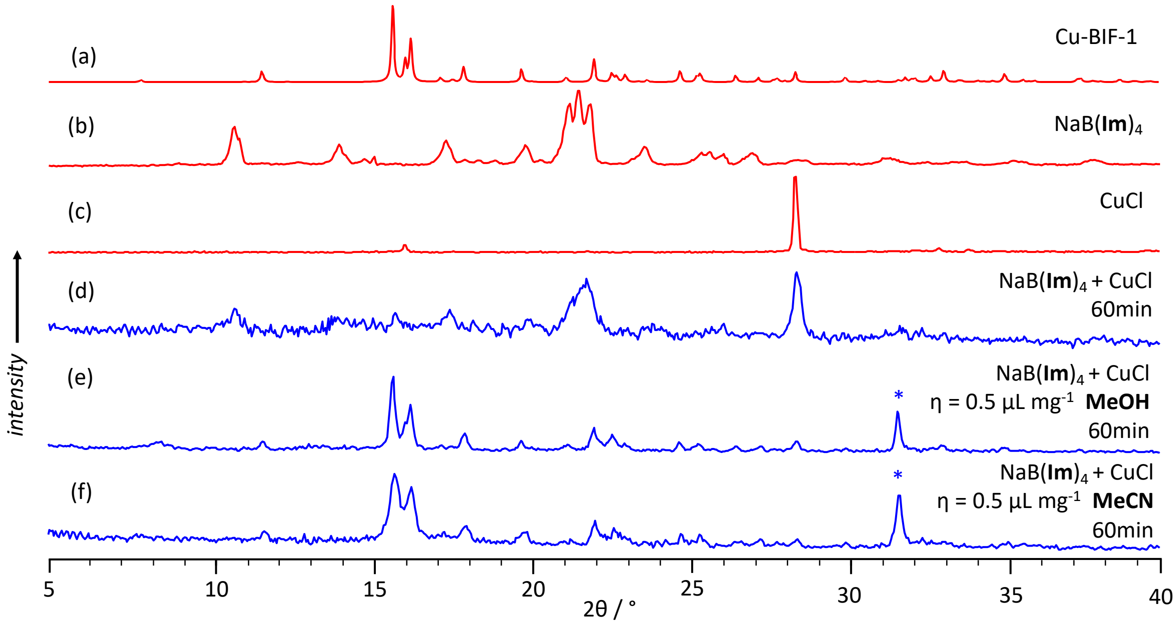

Figure S2. Selected PXRD patterns for neat grinding and LAG of Na[B(**Im**)$_4$] and CuCl to form Cu-BIF-1: (a) Cu-BIF-1 (CSD MOXJIT), (b) Na[B(**Im**)$_4$], (c) CuCl, (d) neat milling of CuCl and Na[B(**Im**)$_4$]. Reaction product following LAG with: (e) MeOH (η=0.5 µL mg^{-1}) or (f) MeCN (η=0.5 µL mg^{-1}) for 60 minutes. PXRD analysis indicates complete conversion to Cu-BIF-1 and NaCl. The asterisk highlights a characteristic Bragg reflection of NaCl.

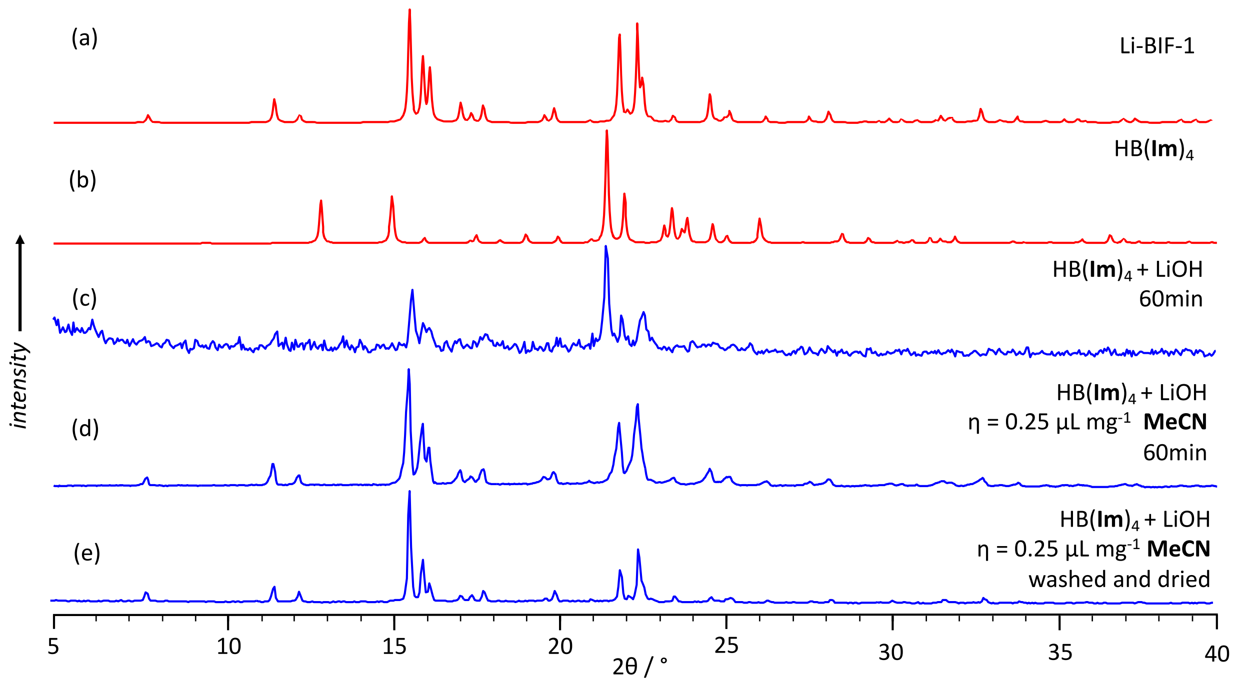

Figure S3. Selected PXRD patterns for neat grinding and LAG of H[B(**Im**)$_4$] and LiOH to form Li-BIF-1: (a) simulated Li-BIF-1 (CSD MOXJEP), (b) simulated for H[B(**Im**)$_4$] (CSD TADHOW), (c) neat milling of LiOH and H[B(**Im**)$_4$]. Product of LAG reaction of H[B(**Im**)$_4$] and LiOH in the presence of MeCN (η=0.25 µL mg^{-1}) after 60 minutes milling: (d) crude material and (e) material after washing with MeCN and drying. PXRD analysis indicates complete conversion to Li-BIF-1.

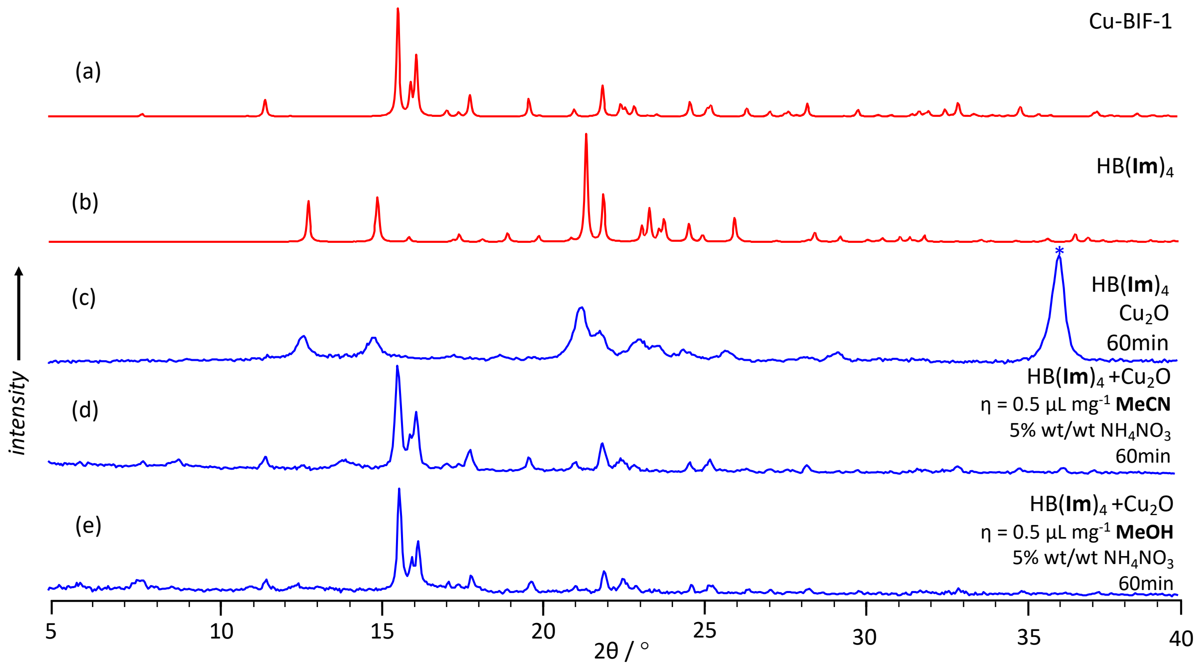

Figure S4. Selected PXRD patterns for neat milling and ILAG of H[B(**Im**)$_4$] and Cu$_2$O to form Cu-BIF-1: (a) simulated Cu-BIF-1 (CSD MOXJIT), (b) simulated for H[B(**Im**)$_4$] (CSD TADHOW), (c) product of neat milling of Cu$_2$O and H[B(**Im**)$_4$]. Product of ILAG reaction of H[B(**Im**)$_4$] and Cu$_2$O in the presence of 5% NH$_4$NO$_3$ by weight, using: (d) MeCN (η=0.5 µL mg^{-1}) and (e) MeOH (η=0.5 µL mg^{-1}) as the liquid additive after 60 minutes milling. PXRD analysis indicates complete conversion to Cu-BIF-1. The asterisk highlights characteristic reflections of Cu$_2$O.

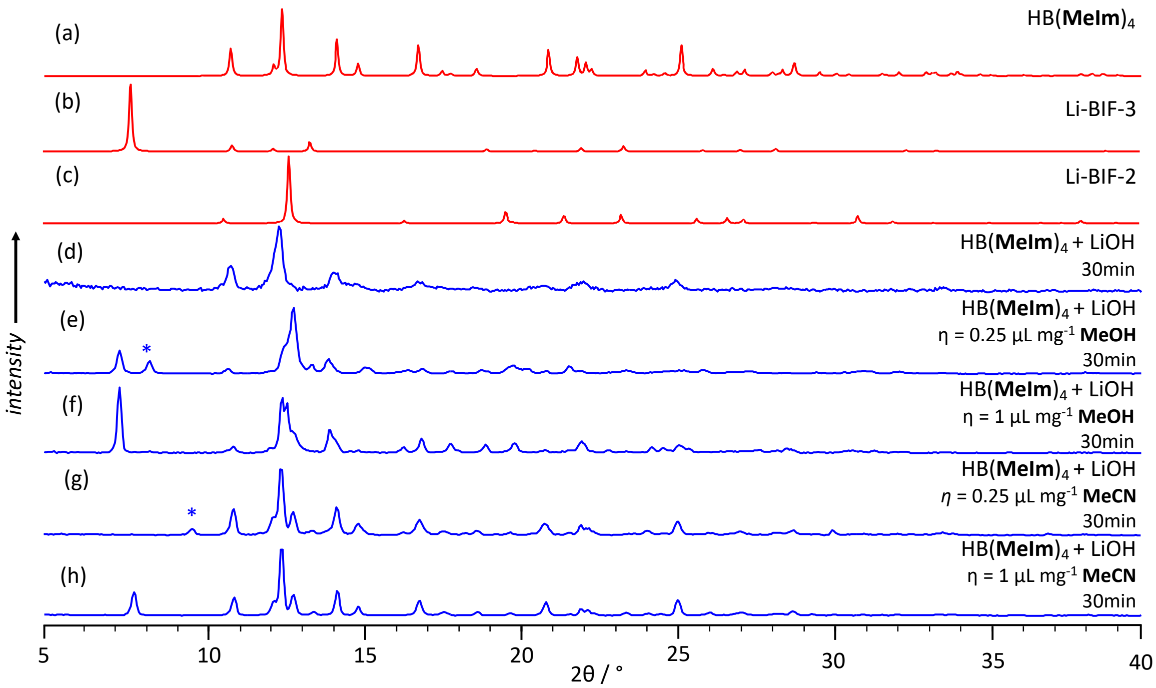

Figure S5. Selected PXRD patterns for LAG of H[B(**Meim**)$_4$] and LiOH to form Li-BIF-2 or Li-BIF-3: (a) simulated for Li-BIF-3 (CSD MUCLOM), (b) simulated for Li-BIF-2 (CSD MOXKUG), (c) simulated for H[B(**Meim**)$_4$] (CSD KUCDOC), (d) product of neat milling LiOH and H[B(**Meim**)$_4$] for 30 minutes. Product of LAG for 30 minutes of H[B(**Meim**)$_4$] and LiOH using: (e) MeOH (η=0.25 µL mg^{-1}), (f) MeOH (η=1 µL mg^{-1}), (g) MeCN (η=0.25 µL mg^{-1}), and (h) MeCN (η=1 µL mg^{-1}). The asterisks indicates Bragg reflections of yet unidentified products. PXRD analysis indicates that neat milling or LAG with either MeOH or MeCN leads to mixtures of Li-BIF-3, Li-BIF-2, H[B(**Meim**)$_4$] and/or a yet not identified phase.

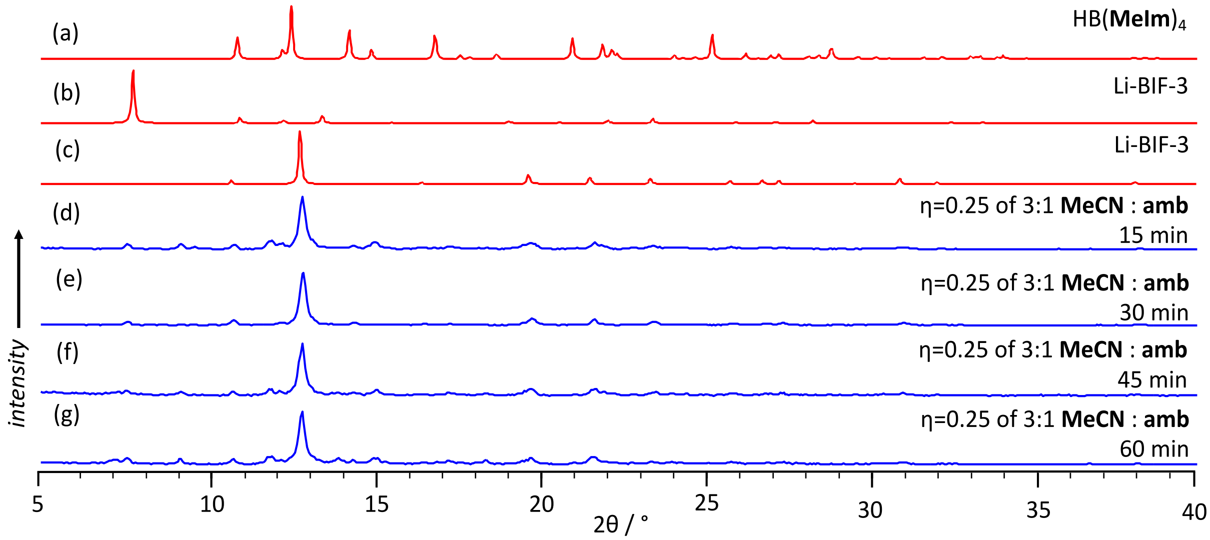

Figure S6. Selected PXRD patterns for LAG of H[B(**Meim**)$_4$] and LiOH to form Li-BIF-2 or Li-BIF-3, using a 3:1 by volume mixture of MeCN and **amb** at η=0.25 µL mg^{-1}: (a) simulated for H[B(**Meim**)$_4$] (CCSD KUCDOC), (b) simulated for Li-BIF-3 (CSD MUCLOM), (c) simulated for Li-BIF-2 (CSD MOXKUG). Reaction mixture after milling for: (d) 15 minutes, (e) 30 minutes, (f) 45 minutes, and (g) 60 minutes. PXRD analysis indicates the formation of Li-BIF-2 as the major product.

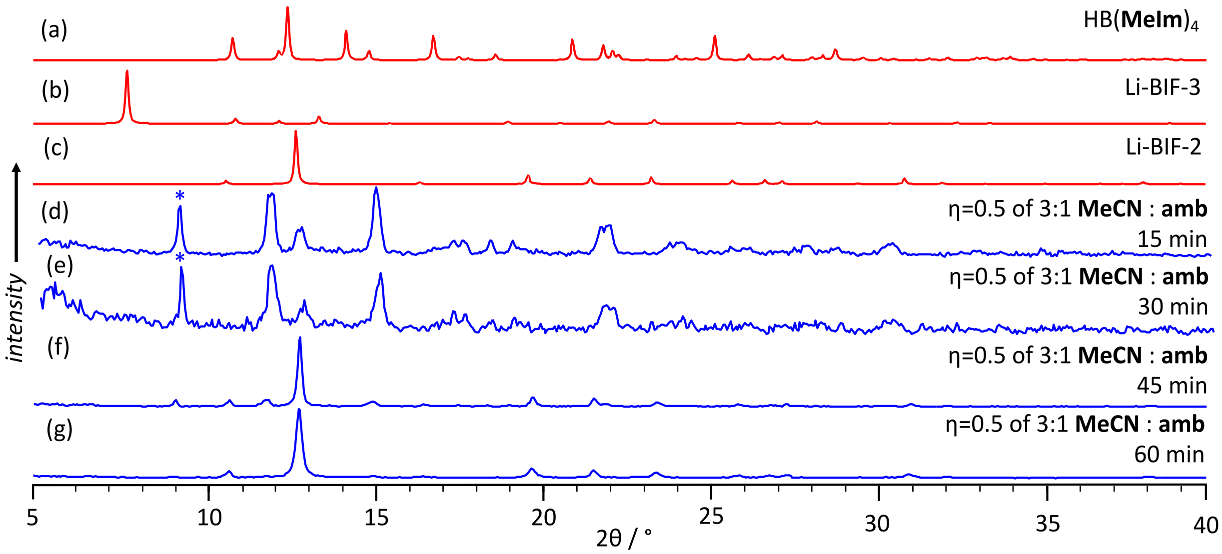

Figure S7. Selected PXRD patterns for LAG of H[B(**Meim**)$_4$] and LiOH to form Li-BIF-2 or Li-BIF-3, using a 3:1 by volume mixture of MeCN and **amb** at η=0.50 µL mg^{-1}: (a) simulated for H[B(**Meim**)$_4$] (CCSD KUCDOC), (b) simulated for Li-BIF-3 (CSD MUCLOM), (c) simulated for Li-BIF-2 (CSD MOXKUG). Reaction mixture after milling for: (d) 15 minutes, (e) 30 minutes, (f) 45 minutes, and (g) 60 minutes. The asterisk highlights an X-ray reflection of a yet unidentified intermediate. PXRD analysis indicates that the final product (g) is dia- Li-BIF-2.

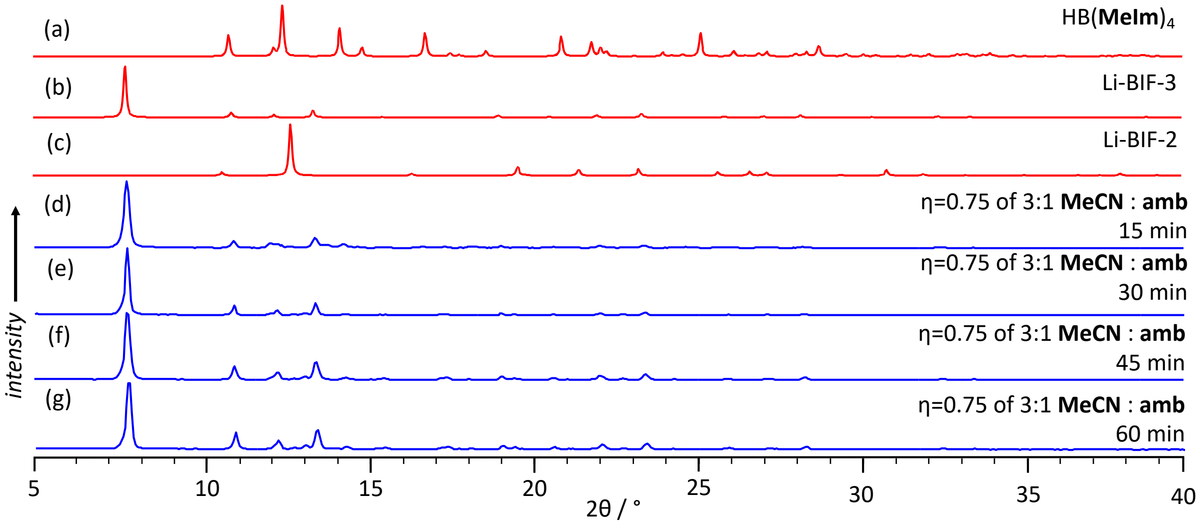

Figure S8. Selected PXRD patterns for LAG of H[B(**Meim**)$_4$] and LiOH to form Li-BIF-2 or Li-BIF-3, using a 3:1 by volume mixture of MeCN and **amb** at η=0.75 µL mg^{-1}: (a) simulated for H[B(**Meim**)$_4$] (CCSD KUCDOC), (b) simulated for Li-BIF-3 (CSD MUCLOM), (c) simulated for Li-BIF-2 (CSD MOXKUG). Reaction mixture after milling for: (d) 15 minutes, (e) 30 minutes, (f) 45 minutes, and (g) 60 minutes. PXRD analysis indicates that this method results in the formation of Li-BIF-3 with small amounts of Li-BIF-2 and residual reactants.

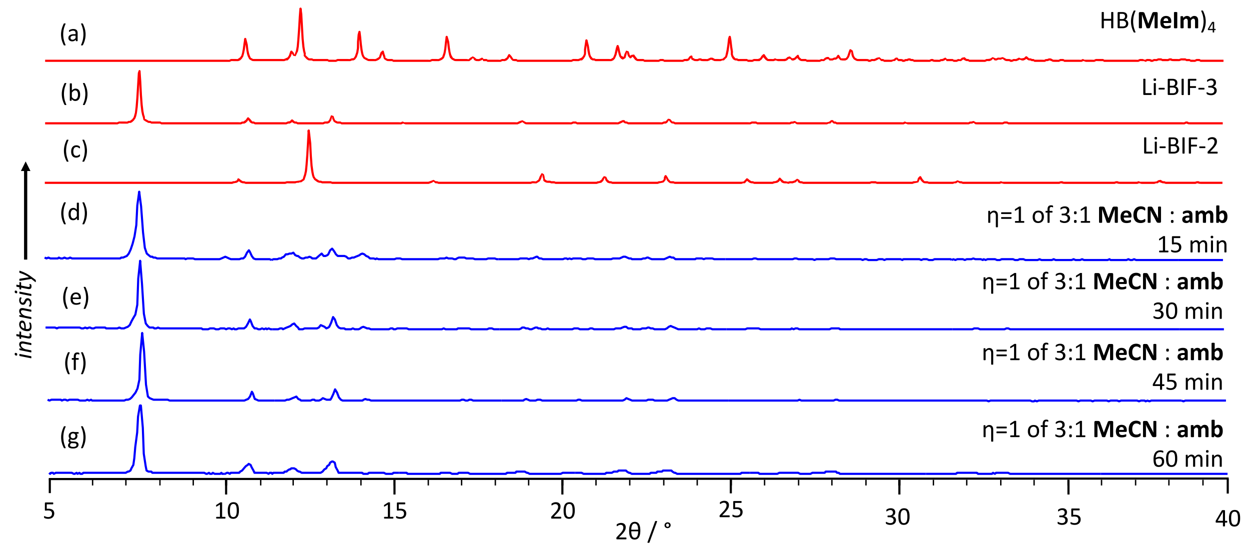

Figure S9. Selected PXRD patterns for LAG of H[B(**Meim**)$_4$] and LiOH to form Li-BIF-2 or Li-BIF-3, using a 3:1 by volume mixture of MeCN and **amb** at *η*=1 µL mg^{-1}: (a) simulated for H[B(**Meim**)$_4$] (CSD KUCDOC), (b) simulated for Li-BIF-3 (CSD MUCLOM), (c) simulated for Li-BIF-2 (CSD MOXKUG). Reaction mixture after milling for: (d) 15 minutes, (e) 30 minutes, (f) 45 minutes, and (g) 60 minutes. PXRD analysis indicates that the final product (g) is SOD-Li-BIF-3.

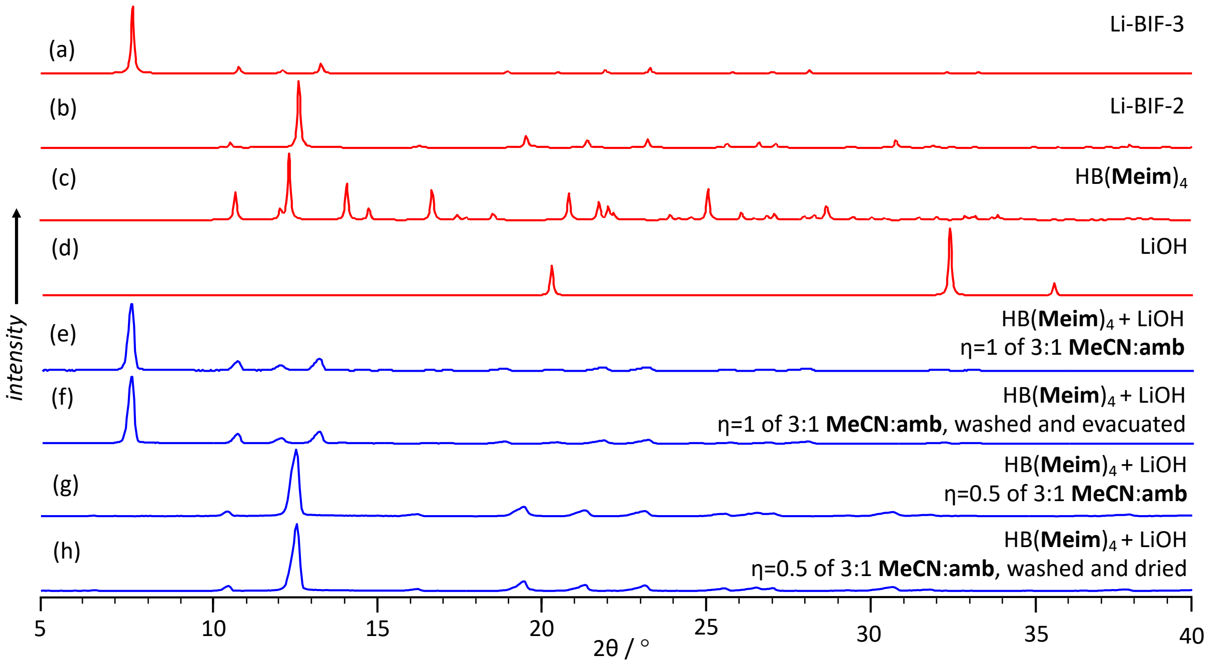

Figure S10. Selected PXRD patterns for mechanochemically prepared Li-BIF-2 and Li-BIF-3, before and after washing: (a) simulated for Li-BIF-3 (CSD MUCLOM), (b) simulated for Li-BIF-2 (CSD MOXKUG), (c) simulated for H[B(**Meim**)$_4$] (CSD KUCDOC), (d) simulated for LiOH (COD ID 1010456), (e) crude Li-BIF-3, (f) Li-BIF-3 after washing with MeCN and evacuation, (g) crude Li-BIF-2, and (h) Li-BIF-2 after washing with MeCN and drying.

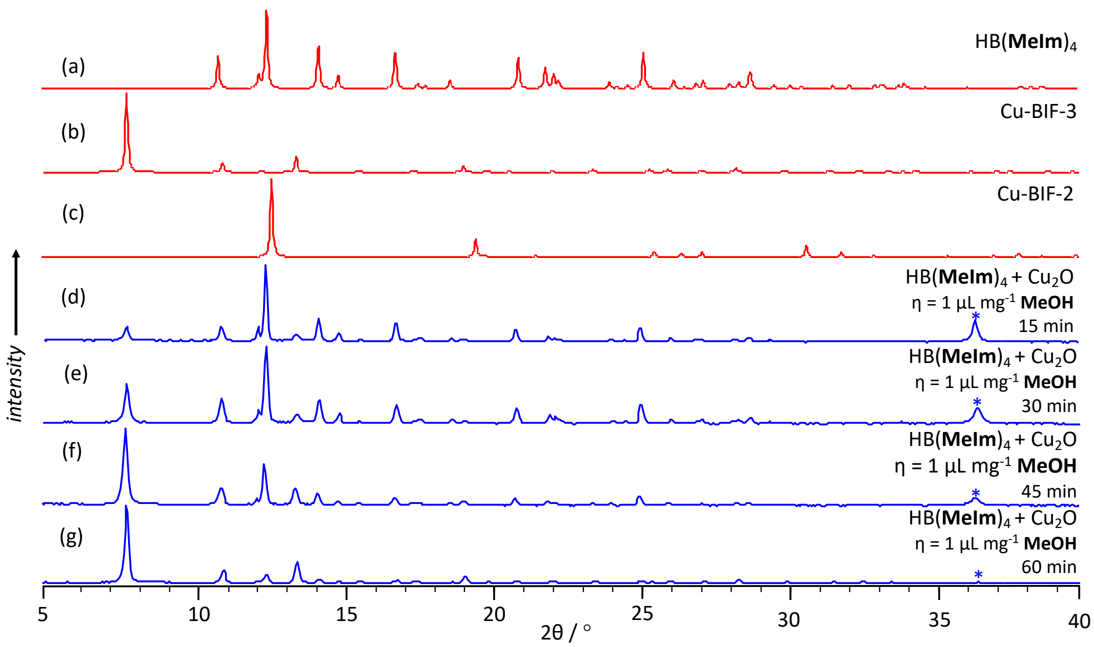

Figure S11. Selected PXRD patterns for LAG of H[B(**Meim**)$_4$] and Cu$_2$O to form Cu-BIF-2 or Cu-BIF-3, using MeOH at η=1 µL mg^{-1}: (a) simulated for H[B(**Meim**)$_4$] (CSD KUCDOC), (b) simulated for Cu-BIF-3 (CSD MOXJOZ), (c) simulated for Cu-BIF-2 (CSD MUCLIG). Reaction mixtures after LAG for: (d) 15 minutes, (e) 30 minutes, (f) 45 minutes, and (g) 60 minutes. PXRD analysis indicates that LAG with MeOH produces Li-BIF-3 with small amount of residual reactants. The asterisks highlight X-ray reflections of Cu$_2$O.

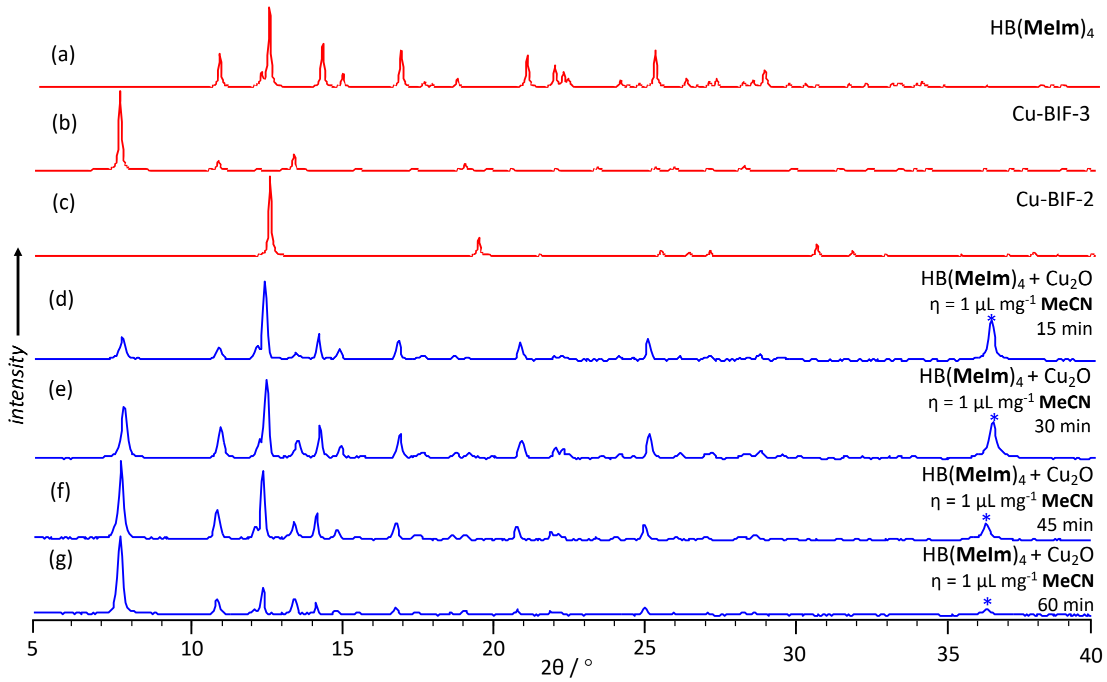

Figure S12. Selected PXRD patterns for LAG of H[B(**Meim**)$_4$] and Cu$_2$O to form Cu-BIF-2 or Cu-BIF-3, using MeCN at η=1 µL mg^{-1}: (a) simulated for H[B(**Meim**)$_4$] (CSD KUCDOC), (b) simulated for Cu-BIF-3 (CSD MOXJOZ), (c) simulated for Cu-BIF-2 (CSD MUCLIG). Reaction mixtures after LAG for: (d) 15 minutes, (e) 30 minutes, (f) 45 minutes, and (g) 60 minutes. PXRD analysis indicates that LAG with MeCN produces Li-BIF-3 with a small amount of residual reactant. The asterisks highlight X-ray reflections of Cu$_2$O.

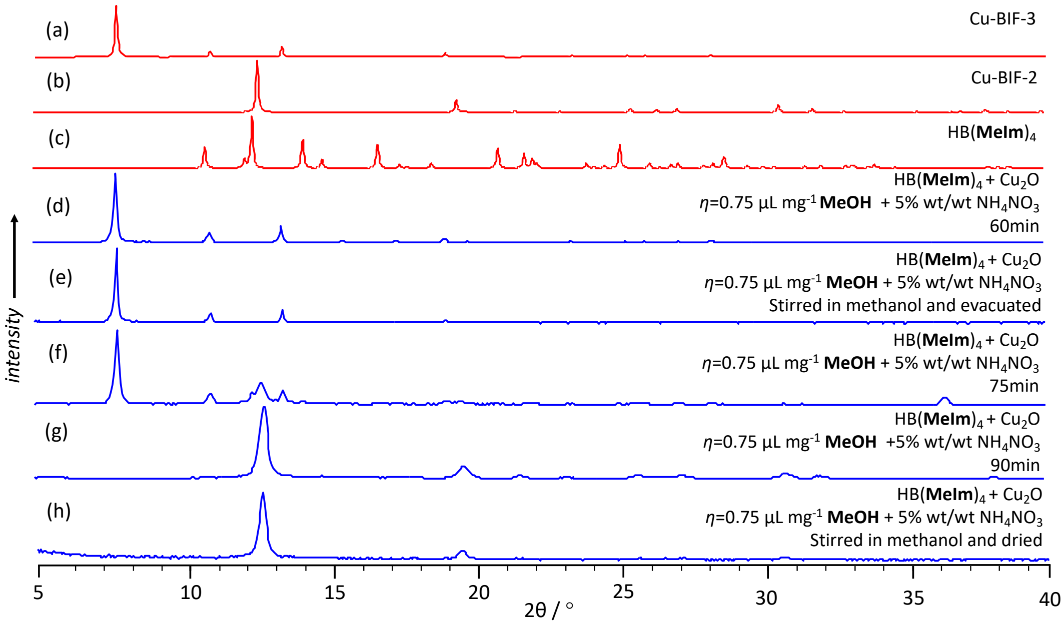

Figure S13. Selected PXRD patterns for Cu-BIF-2 and Cu-BIF-3 before and after washing, made mechanochemically by ILAG with MeOH (η=0.75 mL mg^{-1}) and NH_4NO_3 (5% by weight): (a) simulated for Cu-BIF-3 (CSD MOXJOZ), (b) simulated for Cu-BIF-2 (CSD MUCLIG), (c) simulated for H[B(**MeIm**)$_4$] (CSD KUCDOC), (d) crude Cu-BIF-3 after ILAG for 60 min, (e) Cu-BIF-3 after washing with MeOH and evacuation, (f) crude mixture of Cu-BIF-2 and Cu-BIF-3 after ILAG for 75 min, (g) crude Cu-BIF-2 after ILAG for 90 min, (e) Cu-BIF-2 after washing with MeOH and drying. Data shows that ILAG can selectively produce Cu-BIF-3 and Cu-BIF-3, depending on milling time.

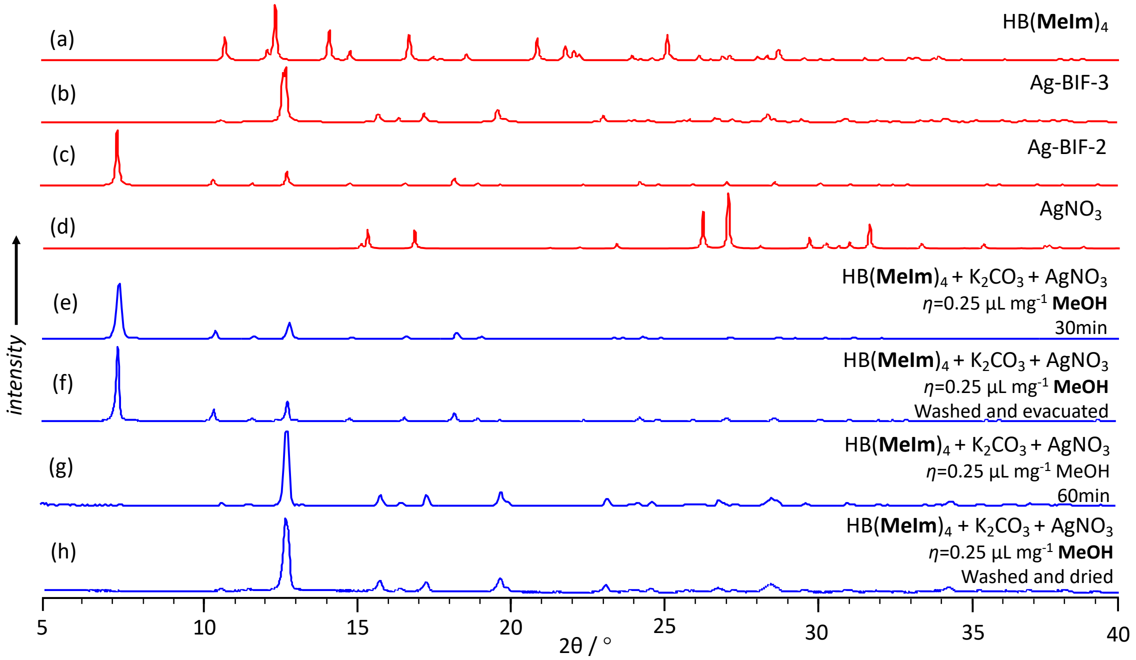

Figure S14. Selected PXRD patterns for Ag-BIF-2 and Ag-BIF-3 samples before and after washing, mechanochemically prepared by LAG with MeOH at η=0.25 mL mg^{-1}: (a) simulated for H[B(**Meim**)$_4$] (CSD KUCDOC), (b) simulated for herein determined structure of Ag-BIF-3, (c) simulated for herein determined structure of Ag-BIF-2, (d) simulated for $AgNO_3$ (COD ID 150468), (e) crude Ag-BIF-3 obtained by 30 minutes LAG, (f) Ag-BIF-3 after washing with cold MeOH, acetone and evacuation, (g) crude Ag-BIF-2 obtained by LAG for 60 minutes, (h) Ag-BIF-2 after washing with cold MeOH, acetone, and drying.

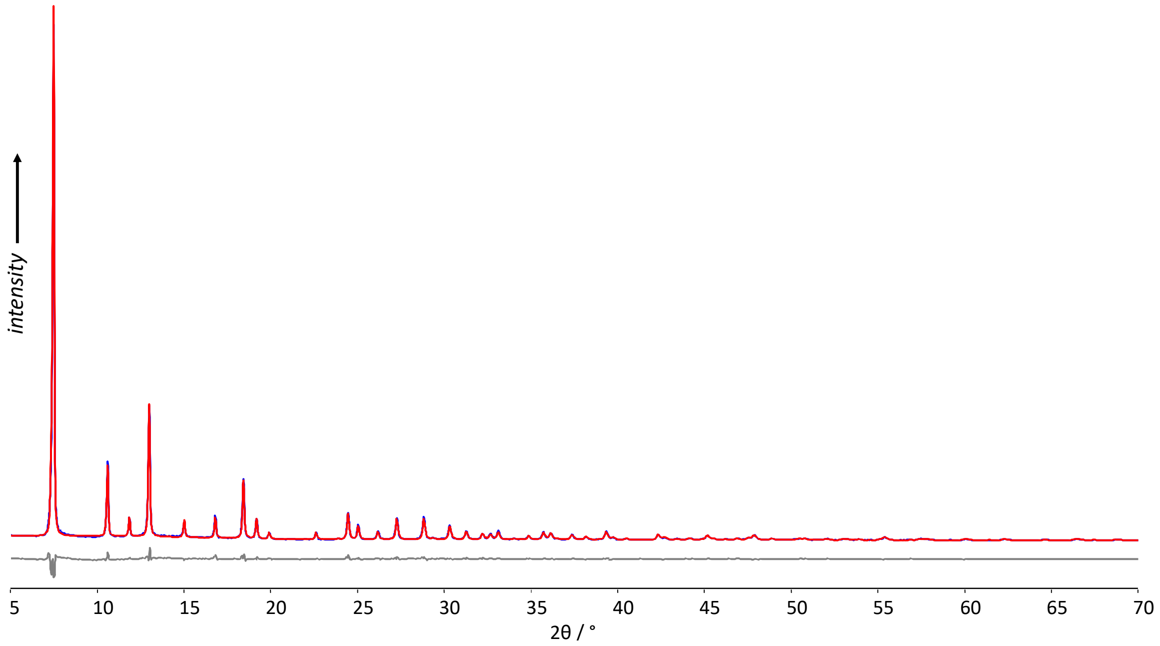

Figure S15. Rietveld refinement plot for Ag-BIF-3 with calculated diffraction pattern in blue, simulated in red and difference plot in grey.

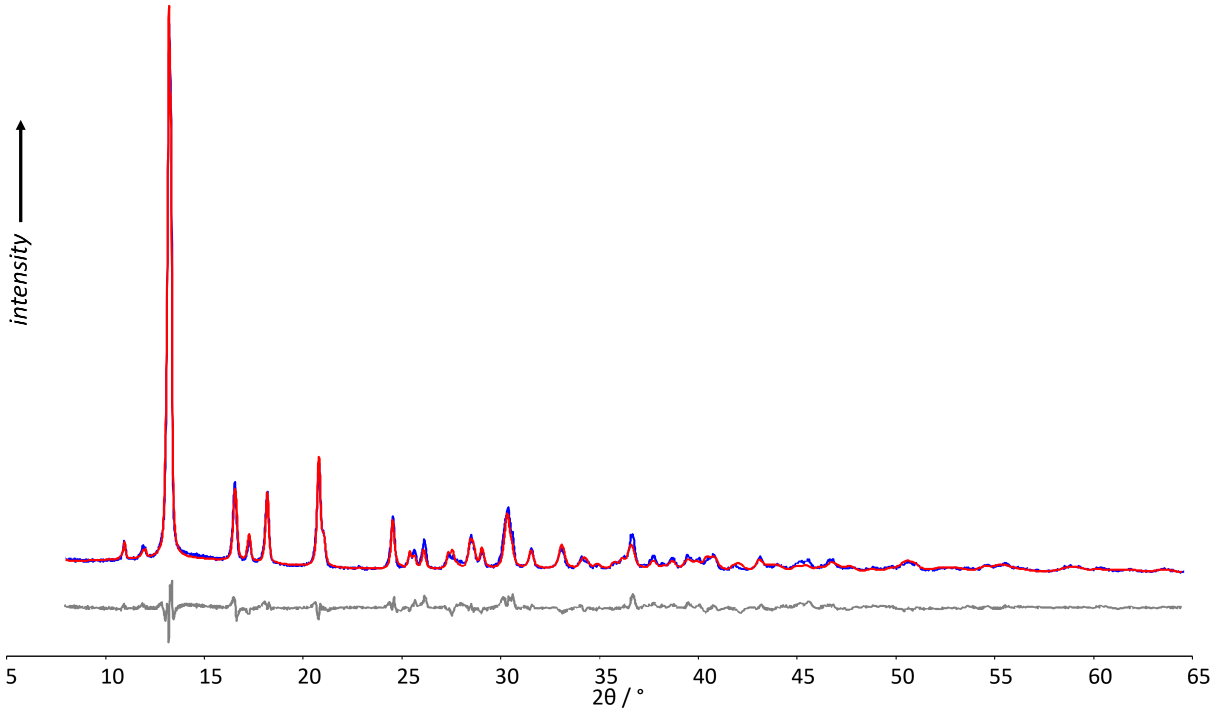

Figure S16. Rietveld refinement plot for Ag-BIF-2 with calculated diffraction pattern in blue, simulated in red and difference plot in grey.

S5 Fourier-transform infrared attenuated total reflectance (FTIR-ATR) spectroscopy

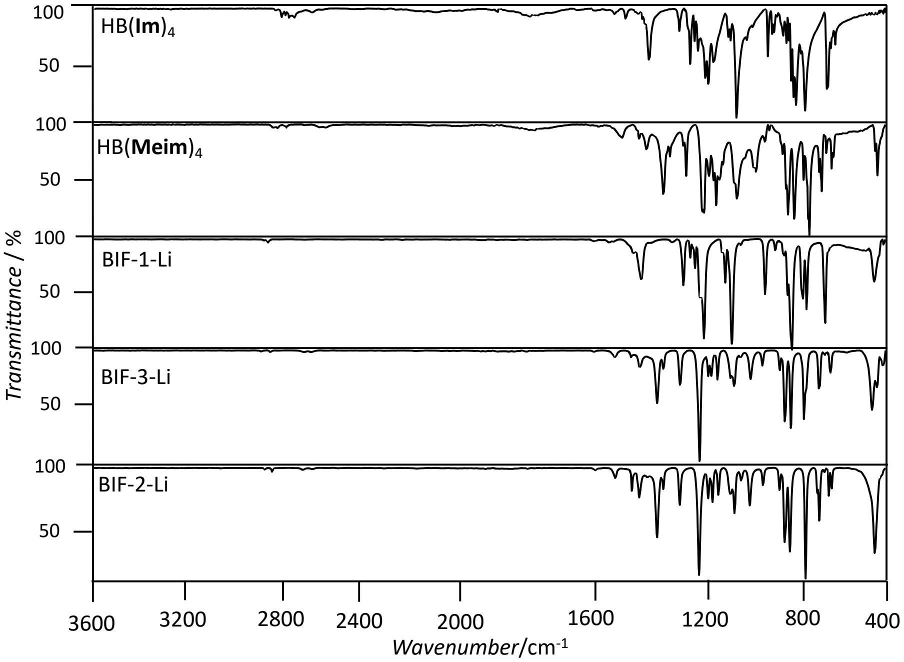

Figure S17. Comparison of FTIR-ATR spectra for mechanochemically prepared Li-based BIFs.

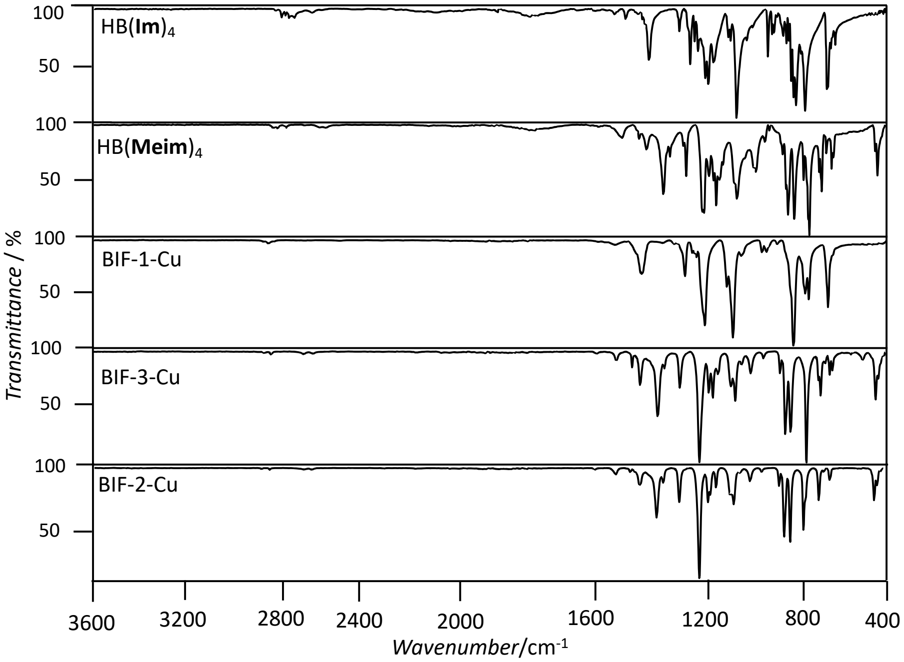

Figure S18. Comparison of FTIR-ATR spectra for mechanochemically prepared Cu-based BIFs.

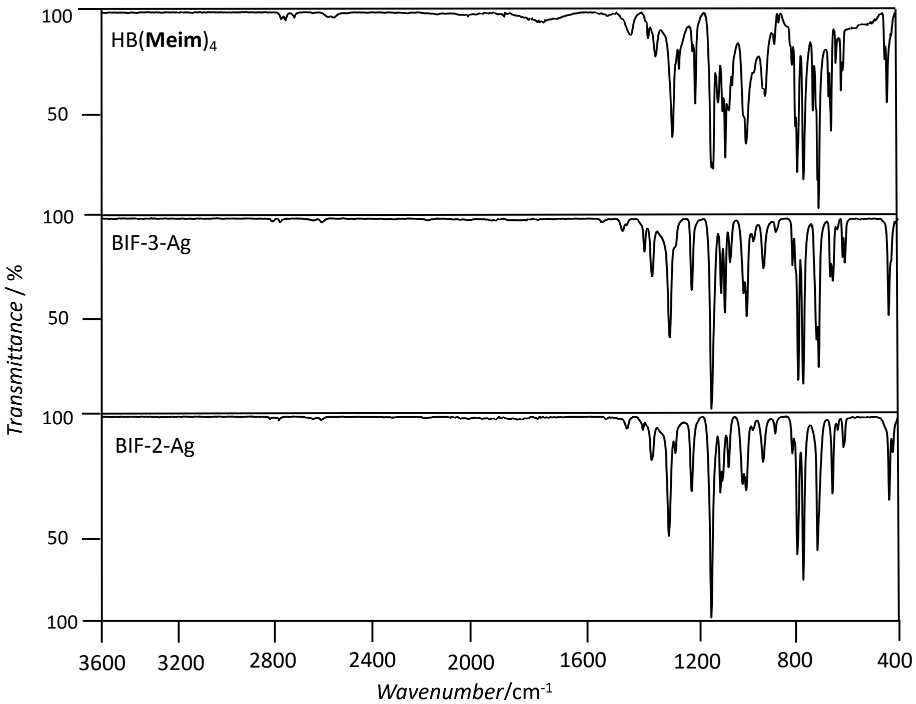

Figure S19. Comparison of FTIR-ATR spectra for mechanochemically prepared Ag-based BIFs.

S6 Thermogravimetric Analysis (TGA)

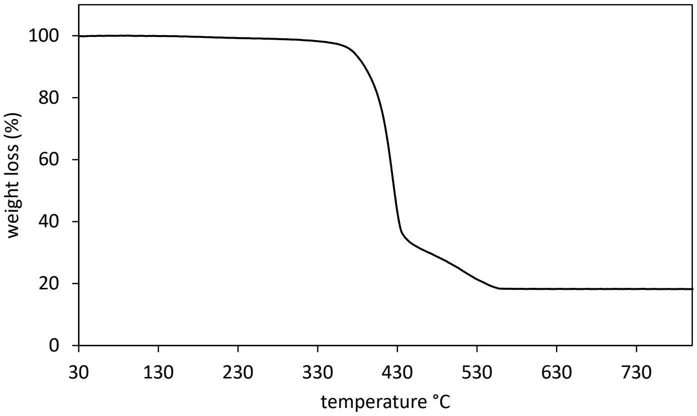

Figure S20. Thermogram for Li-BIF-1 following activation, showing no mass loss before ~330°C. Experimental residue: 18.20, theoretical: 17.40% (calculated based on decomposition to B_2O_3 and Li_2O).

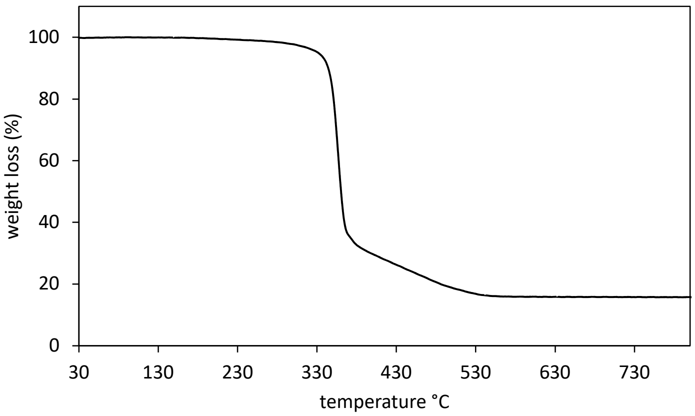

Figure S21. Thermogram for Li-BIF-2 following activation, showing no mass loss before ~330°C. Experimental residue: 15.80%, theoretical: 14.60% (calculated based assumed decomposition to B_2O_3 and Li_2O).

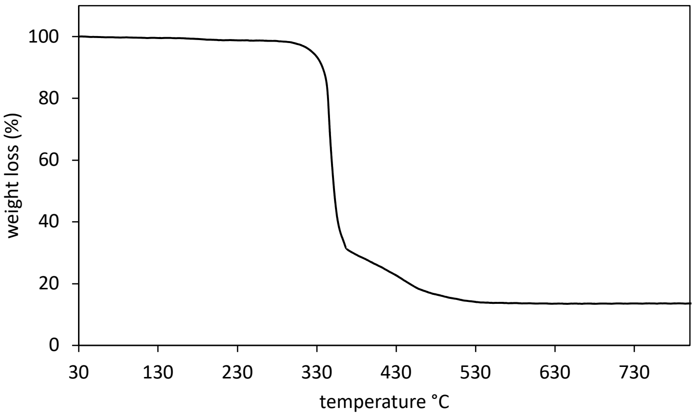

Figure S22. Thermogram for Li-BIF-3 following activation, showing no mass loss before ~300°C. Experimental residue: 14.80 %, theoretical: 14.50 % (calculated based assumed decomposition to B_2O_3 and Li_2O).

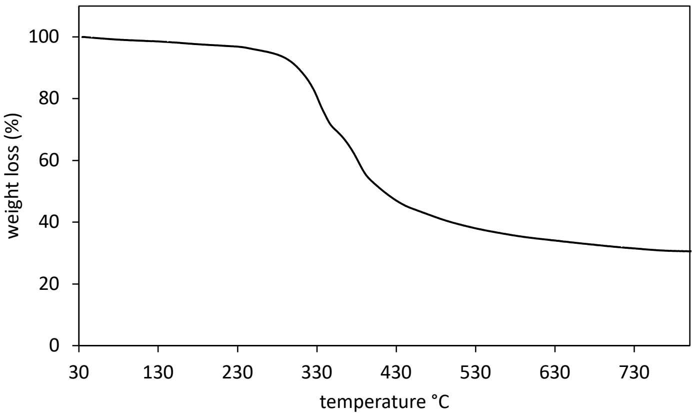

Figure S23. Thermogram for Cu-BIF-1 following activation, experimental residue: 30.80, theoretical: 33.40 (calculated based on decomposition to B_2O_3 and CuO).

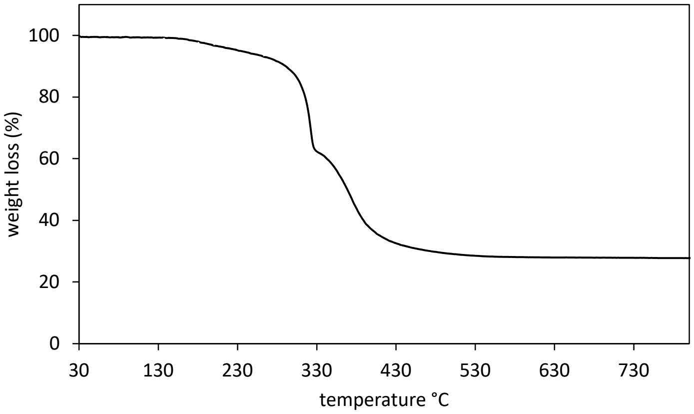

Figure S24. Thermogram for Cu-BIF-2 following activation, showing no mass loss before ~150°C. Experimental residue: 27.80 %, theoretical: 28.70 % (calculated based on decomposition to B_2O_3 and CuO).

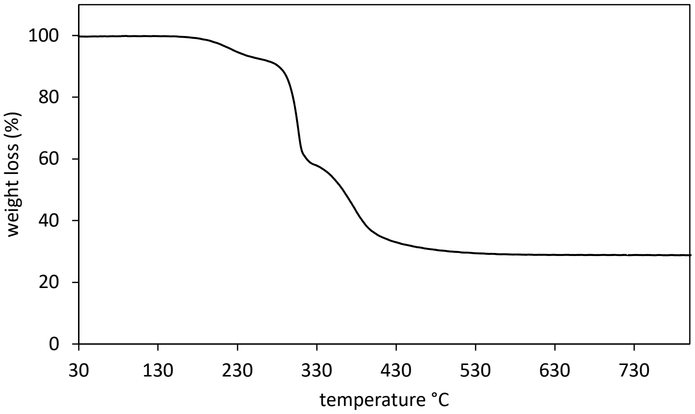

Figure S25. Thermogram for Cu-BIF-3 following activation, showing no mass loss before ~150°C. Experimental residue: 28.80 %, theoretical: 28.70 % (calculated based on decomposition to B_2O_3 and CuO).

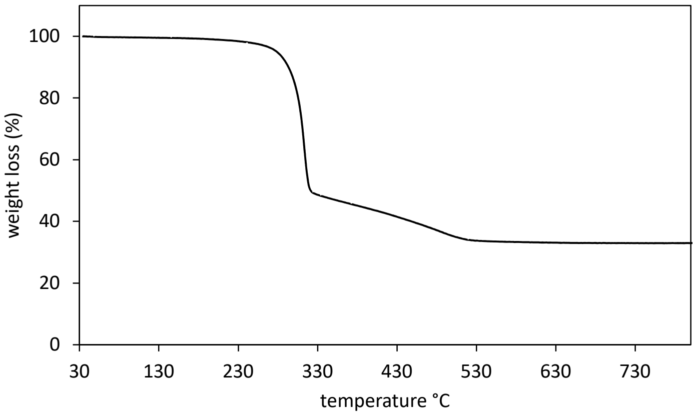

Figure S26. Thermogram for Ag-BIF-2 following activation, showing no mass loss before ~230°C. experimental residue: 33.10 %, theoretical: 32.20 % (calculated based on decomposition to Ag and B_2O_3).

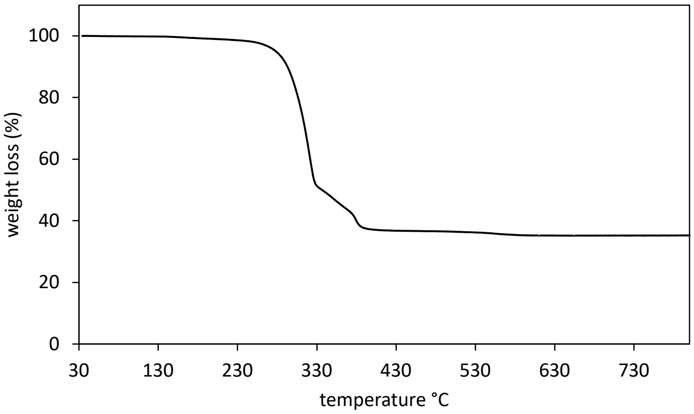

Figure S27. Thermogram for Ag-BIF-3 following activation, showing no mass loss before ~230°C. Experimental residue: 34.60%, theoretical: 32.20% (calculated based on decomposition to Ag and B_2O_3).

S7 Inductively coupled plasma mass spectrometry (ICP-MS)

Table S2. Elemental analysis of metal content in mechanochemically prepared BIFs.

Material	measured metal content (ppb)	expected metal content (ppb)	difference (%)
Li-BIF-1	82.313	83	0.83%
Li-BIF-2	73.010	73	0.01
Li-BIF-3	71.867	73	1.19
Cu-BIF-1	118.866	120.1	1.03
Cu-BIF-2	299.948	300.6	0.22
Cu-BIF-3	270.218	271.2	0.36
Ag-BIF-2	418.405	417.4	0.24
Ag-BIF-3	494.986	492.6	0.48

S8 Surface area measurements

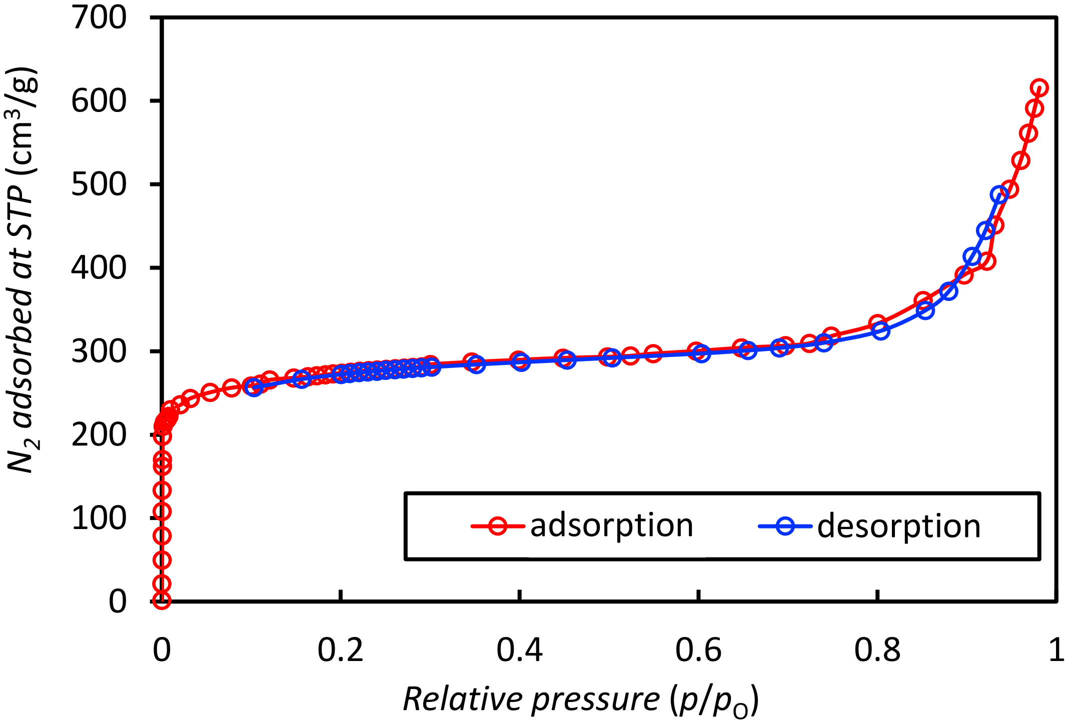

Figure S28. BET isotherm of mechanochemically prepared Li-BIF-3 revealing a BET surface area of 1010 m^2 g^{-1}.

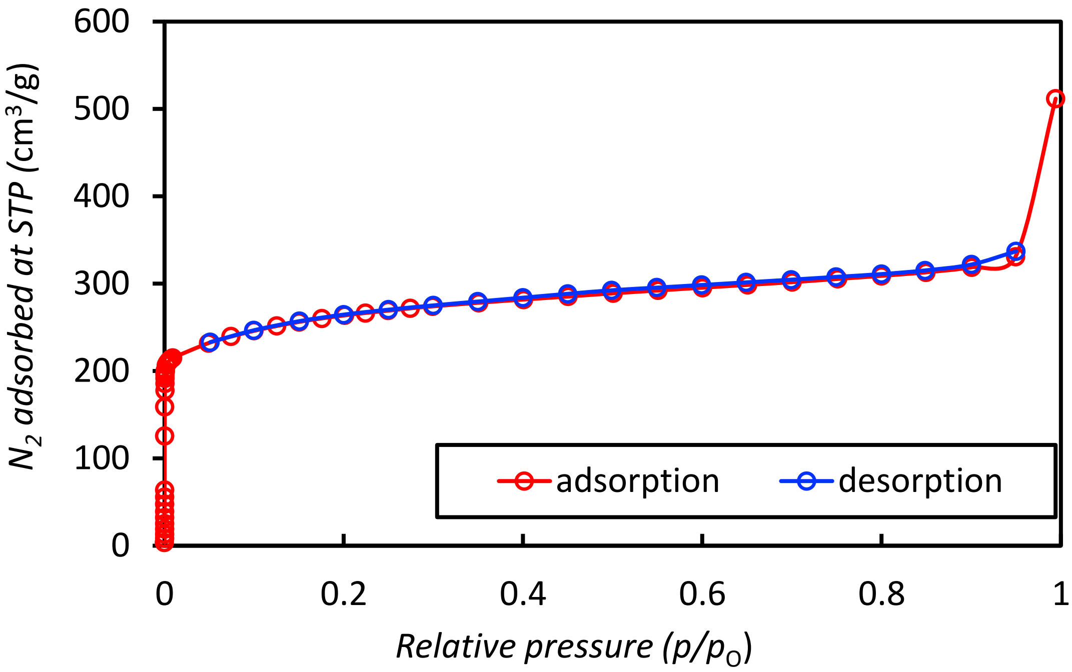

Figure S29. BET isotherm of mechanochemically prepared Cu-BIF-3 revealing a BET surface area of 935 m^2 g^{-1}.

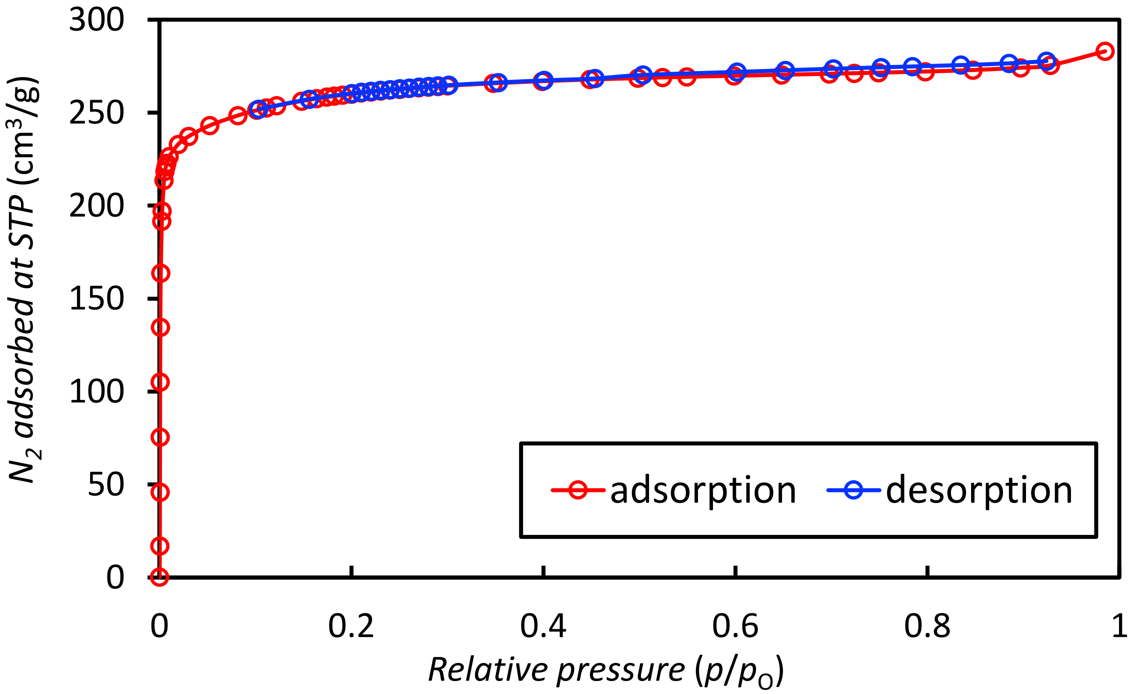

Figure S30. BET isotherm of mechanochemically prepared Ag-BIF-3 revealing a BET surface area of 1020 m^2 g^{-1}.

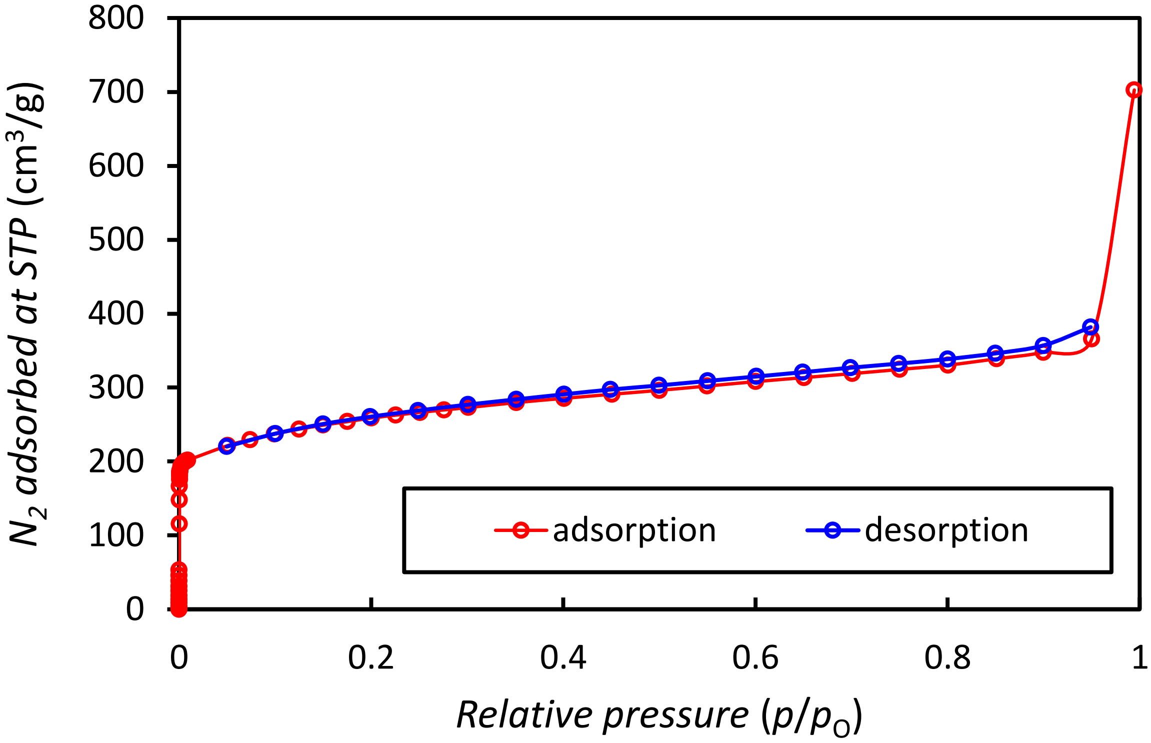

Figure S31. BET isotherm of solution synthesised prepared Cu-BIF-3 revealing a BET surface area of 616 m^2 g^{-1}.[19]

S9 Scanning electron microscopy (SEM)

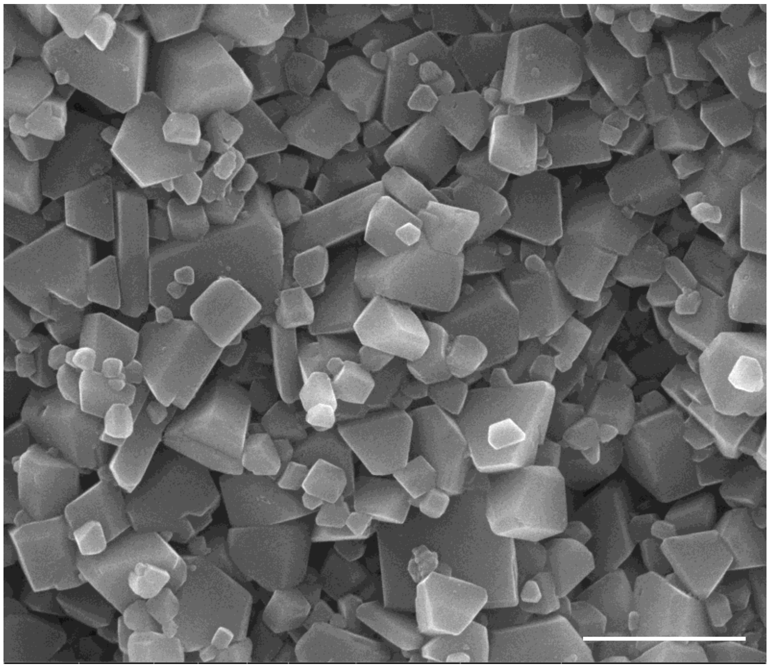

Figure S32. SEM image of mechanochemically prepared Li-BIF-2 with scale bar corresponding to 2 µm shown in white.

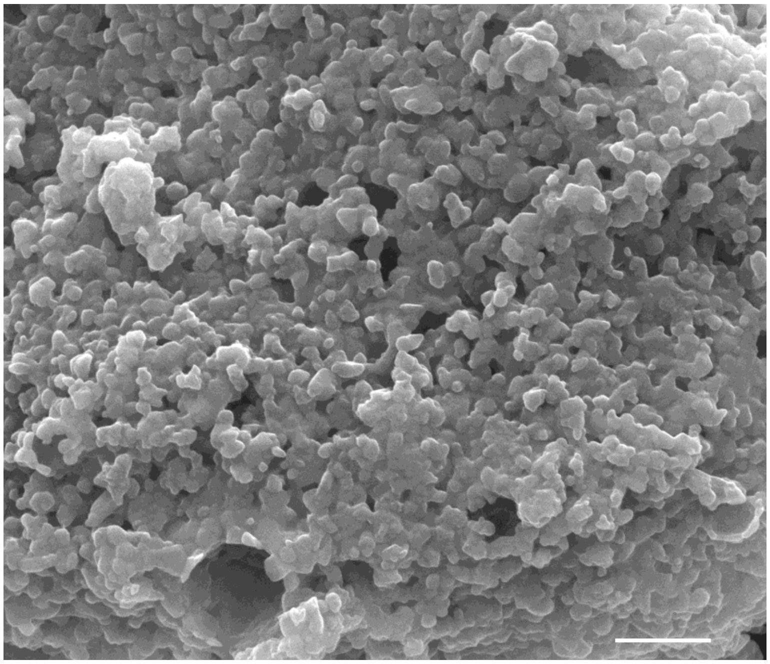

Figure S33. SEM image of mechanochemically prepared Cu-BIF-2 with scale bar corresponding to 1 µm shown in white.

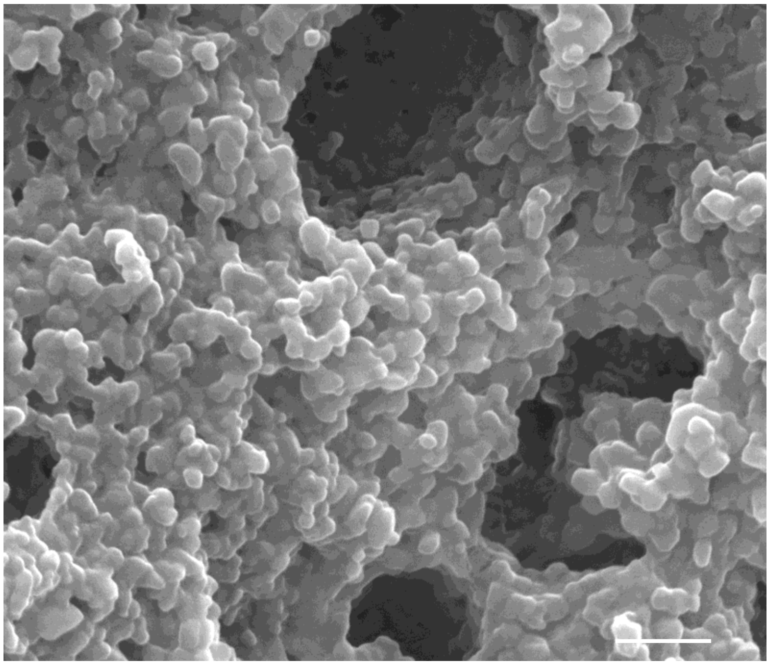

Figure S34. SEM image of mechanochemically prepared Ag-BIF-2 with scale bar corresponding to 500 nm shown in white.

S10 NMR spectroscopy

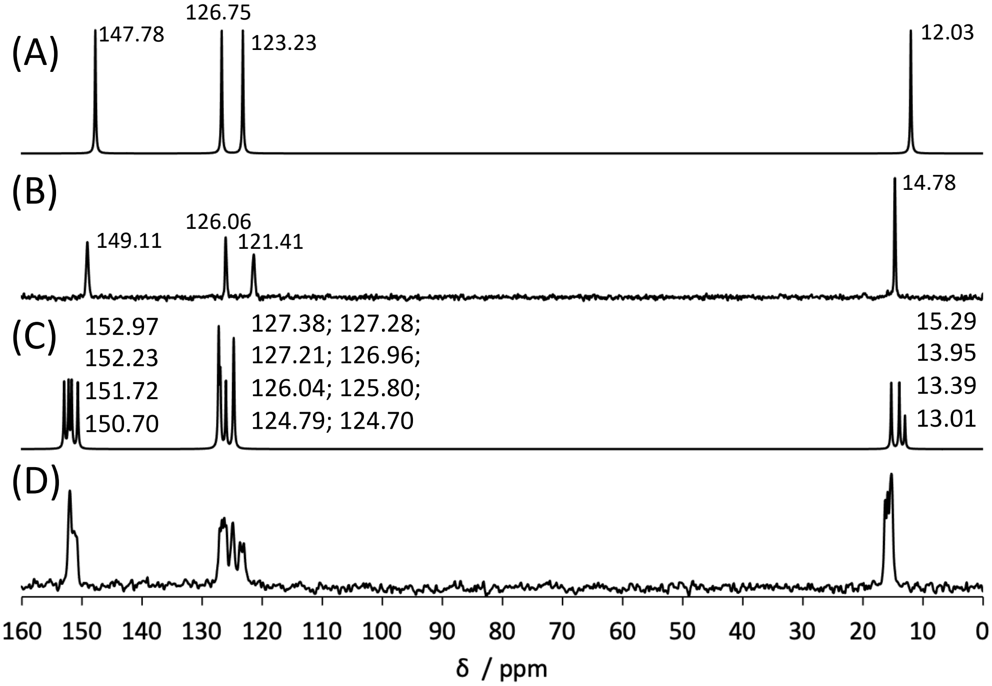

Figure S35. Comparison between (A) calculated ssNMR spectra of Ag-BIF-3, (B) experimental ssNMR spectra of Ag-BIF-3, (C) calculated ssNMR spectra of Ag-BIF-2 and (D) experimental ssNMR spectra of Ag-BIF-2. Chemical shift values are shown for (A) – (C), chemical shift values for (D) shown in Figure S 35 – Figure S-37 and were evaluated using MestReNova.

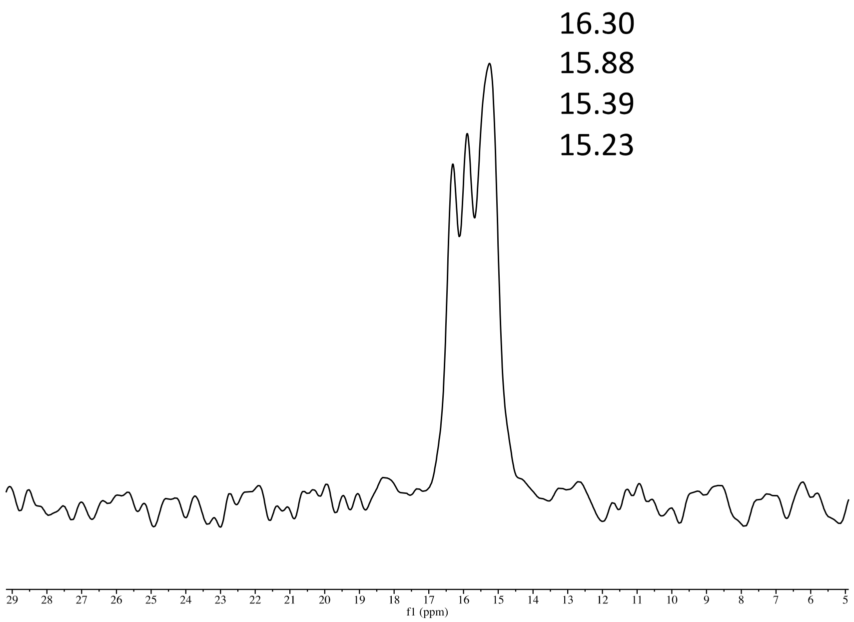

Figure S36. Zoom in of experimental ssNMR spectra for Ag-BIF-2 showing splitting corresponding to 4 distinct CH_3 groups from 4 distinct 2-methylimidazole units, with corresponding chemical shift values shown which were evaluated using MestReNova.

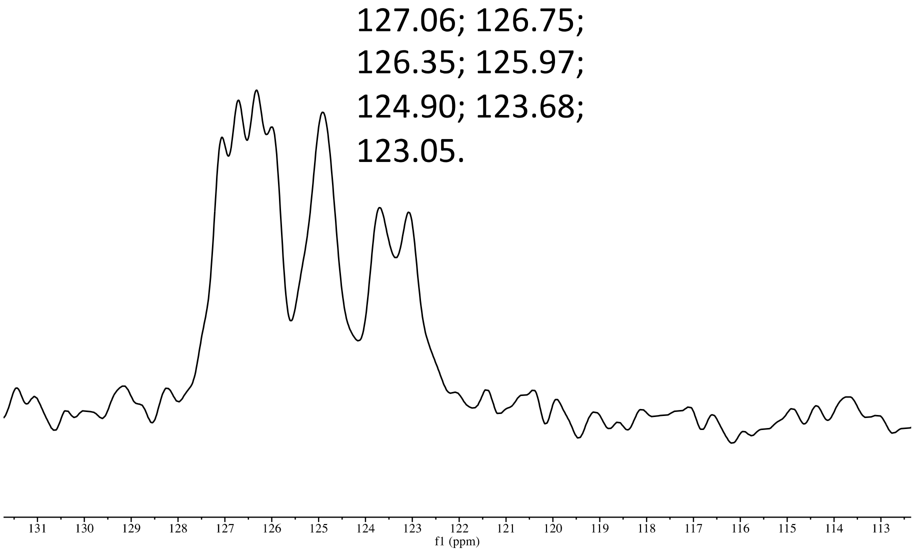

Figure S37. Zoom in of experimental ssNMR spectra for Ag-BIF-2 showing splitting corresponding to the 4 distinct 2-methylimdiazolate linkers with corresponding chemical shift values shown which were evaluated using MestReNova.

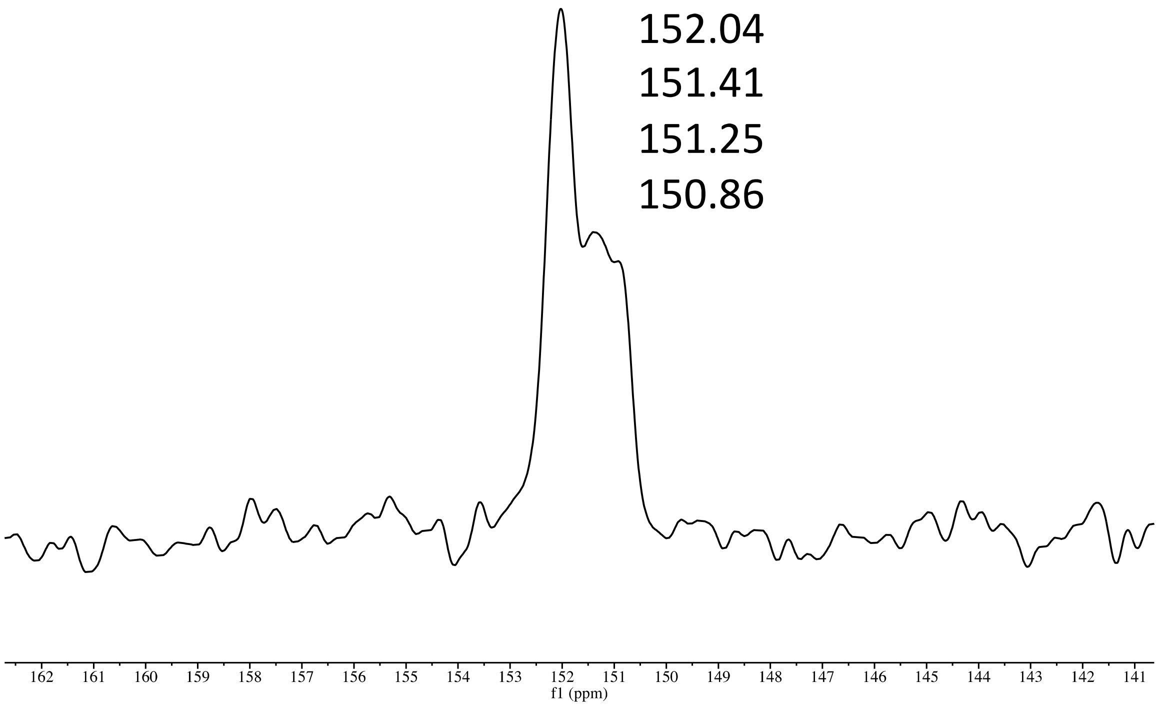

Figure S38. Zoom in of experimental ssNMR spectra for Ag-BIF-2 corresponding to splitting from the 4 distinct 2-methylimidazolate linkers with corresponding chemical shift values shown which were evaluated using MestReNova.

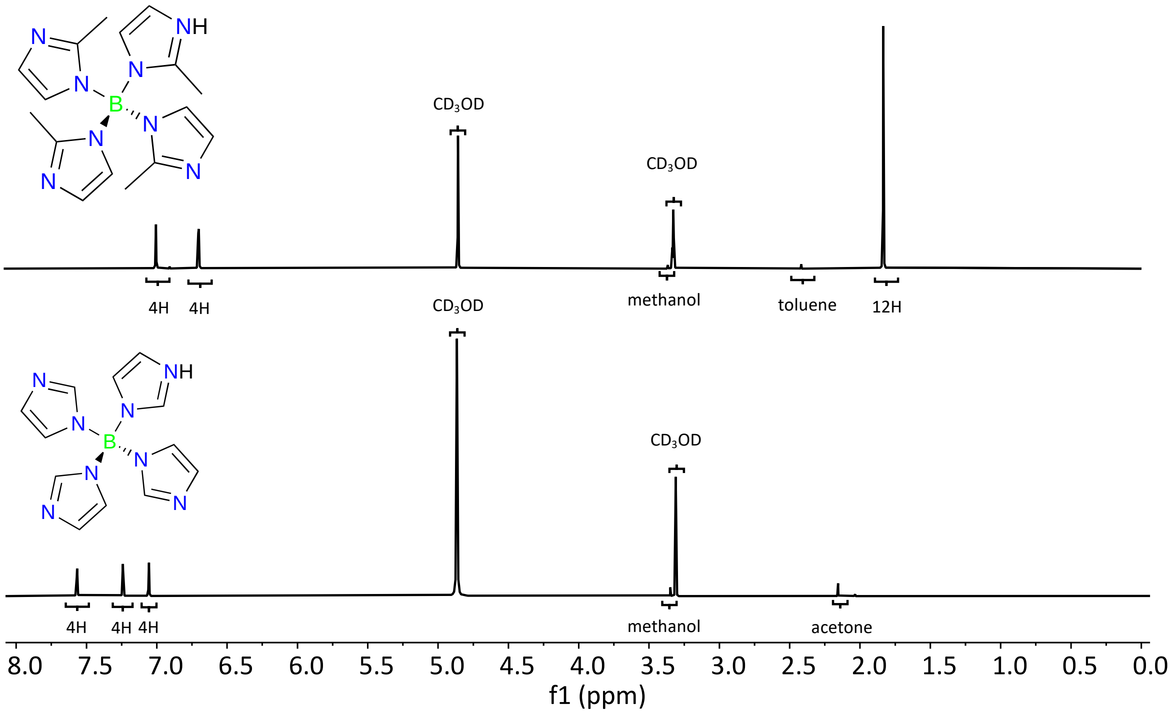

Figure S39. Experimental NMR of (top) HB(**Meim**)$_4$ and (bellow) HB(**Im**)$_4$.

S11 References

1. P. J. Bailey, D. Lorono-Gonzales, C. McCormack, F. Millican, S. Parsons, R. Pfeifer, P. P. Pinho, F. Rudolphi, A. Sanchez Perucha, *Chem. Eur. J.*, 2006, **12**, 5293–5300.
2. S. J. Clark, M. D. Segall, C. J. Pickard, P. J. Hasnip, M. I. J. Probert, K. Refson, M. C. Payne, *Z. Krist.*, 2009, **220**, 567-570.
3. T. Björkman, *Comput. Phys. Commun*. 2011, **182**, 1183–1186.
4. J. P. Perdew, K. Burke, M. Ernzerhof, *Phys. Rev. Lett.* 1996, **77**, 3865–3868.
5. A. Tkatchenko, R. A. DiStasio, R. Car, M. Scheffler, *Phys. Rev. Lett.* 2012, **108**, 236402.
6. A. Ambrosetti, A. M. Reilly, R. A. DiStasio, A. Tkatchenko, *J. Chem. Phys.* 2014, **140**, 18A508.
7. A. M. Reilly, A. Tkatchenko, *Chem. Sci.* 2015, **6**, 3289–3301.
8. H. J. Monkhorst, J. D. Pack, *Phys. Rev. B* 1976, **13**, 5188–5192.
9. J. R. Yates, C. J. Pickard, F. Mauri, *Phys. Rev. B* 2007, **76**, 024401.
10. A. Boultif, D. Louër, *J. Appl. Crystallogr.* 2004, **37**, 724–731.
11. A. Le Bail, H. Suroy, J. L. Fourquet, *Mat. Res. Bull.* 1988, **23**, 447–452.
12. H. M. Rietveld, *Acta Crystallogr.* 1967, **22**, 151–152.
13. A. A. Coelho, *J. Appl. Cryst.*, 2018, **51**, 210-218.
14. G. S. Pawley, *J. Appl. Crystallogr.* 1981, **14**, 357–361.
15. Bruker. *APEX3*; Bruker AXS Inc.: Madison, Wisconsin, USA, 2012.
16. L. Krause, R. Herbst-Irmer, G. M. Sheldrick, D. Stalke, *J. Appl. Cryst.* 2015, **48**, 3–10.
17. G. M. Sheldrick, *Acta Cryst.* **2015**, *A71*, 3-8.
18. G. M. Sheldrick, Acta Cryst. **2015**, *C71*, 38.
19. J. Zhang, T. Wu, C. Zhou, S. Chen, P. Feng and X. Bu, *Angew. Chem. Int. Ed.*, 2009, **48**, 2542-2545.